A CONTINUOUS VORTICITY PANEL METHOD FOR THE PREDICTION OF STEADY AERODYNAMIC LOADS ON LIFTING SURFACES

by

ALBERT TIENGTSUNG YEN

Dissertation submitted to the Graduate Faculty of the
Virginia Polytechnic Institute and State University
in partial fulfillment of the requirements for the degree of
DOCTOR OF PHILOSOPHY
in
Engineering Science and Mechanics

APPROVED:

Ali H. Nayfeh, Co-Chairman

Dean T. Mook, Co-Chairman

William S. Saric

Demetri P. Telionis

Layne T. Watson

January, 1982

Blacksburg, Virginia

ACKNOWLEDGEMENTS

The author wishes to express his deep gratitude to Professors Nayfeh and Mook for their invaluable suggestions and criticisms, for many helpful ideas, and for guidance and encouragement in the pursuance of this dissertation. The author would also like to use this opportunity to thank Professors Saric, Telionis, and Watson for their help during the course of this research.

Most of all, infinite thanks are owed to my wife, , and my parents for their constant inspiration, encouragement, and patience. Therefore, I humbly dedicate this work to my parents and wife.

This research was sponsored by NASA-Langley Research Center and Army Research Office under Grant NSG-1262.

TABLE OF CONTENTS

LIST OF FIGURES

Chapter I

INTRODUCTION AND LITERATURE REVIEW

1.1 INTRODUCTION

Many modern aircraft and missiles designed for supersonic speeds employ highly swept, low-aspect, delta and delta-like wings with sharp or thin edges. Within the flight envelopes of such wings are conditions of subsonic speeds and high angles of attack. To accurately predict the aerodynamic characteristics under these conditions has been a long-standing problem. One of the principal features of high-angle-of-attack aerodynamics is that the lift and pitching moment are no longer linear functions of the angle of attack. This is partly attributed to the separation of the flow from the leading edges of the lifting surfaces. This separation is responsible for the formation of a vortex sheet that rolls up above the wing and contributes to a strong spanwise, or crossflow, component of velocity on the upper surface. Therefore, a very favorable pressure gradient is generated, which greatly reduces the tendency of the boundary layer to separate from the surface of the wing. This makes it possible to fly at high angles of attack

without aerodynamic stall. Also, the strong spanwise component of velocity greatly increases the speed on the upper surface and thereby is responsible for a significant contribution to the lift. The actual lift can be more than twice as much as that predicted by a linear aerodynamic theory that fails to account for leading edge separation.

The purpose of the present work is to develop a method to predict not only the total and distributed aerodynamic loads but also the vorticity fields on lifting surfaces having sharp-edge separation in a steady, subsonic, and inviscid flow. The lifting surface is not restricted by aspect ratios, angles of attack, planforms, or camber. In order to achieve this purpose, continuous vorticity panels have been placed on the wing. Also, the shapes of the wakes emanating from the sharp edges of the lifting surfaces and the vortex cores in the wakes have been obtained as part of the solution.

1.2 LITERATURE REVIEW

From the very beginning of the exploration of the flow over slender wings at large angles of attack the experimental work has exhibited the nonlinear aerodynamic characteristics over the angle-of-attack range. These nonlinear relationships were found by many experimentalists.

These experimental studies of the vortex sheet separating from the sharp edges of slender wings revealed at least three distinct cores and lines of separation in the flowfields. The flows leaving the sharp edges from the upper and lower surfaces of the wing form free-shear layers. The separated free-shear layers joining the leading edges of the wing roll up spirally to form two vortex cores above the upper surface of the wing. This is known as the primary vortex; it has the dominating effect on the nonlinear relationship between the total aerodynamic load and the angle of attack.

Due to the leading-edge vortices the flow at the wing surface is directed outwards. A small secondary vortex is formed by the steep pressure gradient between the minimum of pressure and the leading-edge. The secondary vortex rolls up spirally in anopposite sense to that of the primary vortex. In the range of moderate to large angles of attack, the strength of the secondary vortex core was found to be much smaller than that of the primary core.

The third vortex core and separation line may occur between the lines of secondary and primary separation. The tertiary vortex is relatively very small.

Maskell [1], and Peckham [2] found that the shape and strength of the primary vortex are relatively independent of

Reynolds number. This relative independence of the viscous effect suggests that the flow field can be analyzed by using an inviscid model.

The earliest attempt to describe qualitatively the vorticity distribution in a delta wing with leading-edge separation is due to Elle and Jones [3]. They mentioned that the leading-edge vortices are much stronger and move inboard at high angles of attack so that the flow pattern is dominated by the separations. As a result, the vortex lines run spanwise for a short distance on either side of the centre line and then turn forward almost through 90 degrees. Before the vortex lines cross the leading edges, they nearly turn through a right angle. The vortex lines cover the triangular regions near the wing tips by crossing the leading edges and the trailing edge. This vorticity distribution is shown in Fig. 1. Mangler and Smith [4] found that the strength of the resulting reversed trailing vorticity is about 15 per cent of that of the leading edge vortex. A detailed comparison between laminar boundary-layer and turbulent boundary-layer theory for the vorticity distribution on the upper surface of a delta wing has been made by Hummel [5]. It suggests that the pressure distributions calculated by using inviscid models should be compared with the experimental results corresponding to a turbulent boundary-layer flow.

Francis and Kennedy [6] investigated the nature of the near surface bound vorticity distribution for rectangular wings. They found that the vortex lines leaving the surface layer at points of separation interact with one another and roll up to form spiral shaped vortices whose evolution is dependent on the local tip geometry and orientation. The general shapes of the array of the vortex lines is qualitatively similar to that hypothesized in Prandtl lifting-line theory [7].

For an exhaustive review of the linear approaches, the reader is referred to the articles of Ashley and Rodden [8], and Belotserkovskii [9].

A very early nonlinear theory for rectangular wings was presented by Bollay [10]. He studied the case of rectangular wings with aspect ratios less than one. Although his method gives good results, it cannot treat the case of slender wings with arbitrary planform. Later, Gersten [11] assumed that the free vortex lines leave the wing outside the wing plane in his nonlinear theory for slender wings having general planforms and arbitrary aspect ratios. However, this method cannot describe the detailed flow situation so that the pressure distribution cannot be predicted.

The leading-edge suction analogy presented by Polhamus [12] provides a method suitable for calculating the

nonlinear aerodynamic characteristics of wings with pointed tips and side edges. The suction analogy assumes that the normal force needed for the flow around a leading edge to reattach to the wing is equivalent to the leading-edge suction force required to maintain the flow attached to the leading edge in an unseparated condition. The unseparated leading edge suction force is calculated, and is then rotated normal to the wing to obtain the lift contribution of the leading-edge vortex. The overall characteristics of slender wings can be calculated with remarkable accuracy, but the flow field details and detailed surface pressure distributions cannot be obtained.

Several attempts had been made in the past toward more realistic representations of the physics of the vortex formation by Legendre [13], Brown and Michael [14], Mangler and Smith [15], and Smith [16]. In all these methods the assumption of conical flow is used. These models are able to predict qualitatively the type of pressure distributions that had been observed experimentally. They overpredict the experimental load distribution by a considerable amount toward the trailing edge because the conical theory does not satisfy the Kutta condition at the trailing edge and does not account for the deformation of the leading-edge vortex sheet in the chordwise direction. Many experimentalists such

as Marsden, Simpson and Rainbird [17], and Hummel [18,19] have shown that the flow over swept wings with leading edge vortex separation is nonconical. Therefore, in later years conical flow methods were followed by fully three-dimensional techniques to calculate the nonconical flow and to fulfil the Kutta condition at the wing trailing-edge. There are three types of methods to treat nonconical, fully three-dimensional flow around wings with leading edge separation, namely, single line vortex methods, multiple line vortex methods, and vortex sheet methods. A brief discussion of each is presented below.

Nonconical single line vortex methods are due to Nangia and Hancock [20], and Matoi, Covert, and Widnall [21]. They attempted to satisfy the zero-load, trailing-edge condition on a delta wing in the presence of a separated vortex sheet from the leading edge of slender wings. These spiral vortex sheets from the leading edge are replaced by two concentrated line vortices of variable strength with two feeding "cuts" between the line vortices and the respective leading edges. They developed a numerical collocation method, in that the vorticity distribution is described by continuous functions with unknown coefficients. The leading-edge vortex location is similarly described by functions with unknown coefficients. These unknowns are

found by satisfying the downwash condition and the no-force condition on the leading-edge vortex representation. Due to the nonlinear nature of the boundary conditions with respect to the vortex position, the solution is obtained from an iterative scheme based on Newton's method. They showed that the main features of the loading predicted by the theory tie in encouragingly with the experimental trends.

In the area of the multiple line vortex methods (or nonlinear vortex-lattice methods), Belotserkovskii [22] developed a method to calculate the aerodynamic loads on wings with tip separation. The wing is replaced by a vortex lattice and the wake by a finite number of discrete-vortex lines. Each discrete-vortex line consists of a finite number of straight finite segments and one semi-infinite straight segment. Then, through an iteration procedure, the finite segments in the wake were made parallel to the velocity at their midpoints. He showed that the method gives good results in predicting the total and distributed loads on rectangular wings at large angles of attack. Following Belotserkovskii, Mook and Maddox [23] demonstrated the feasibility of using a discrete-vortex concept to model the steady flowfield past delta wings. To simulate the leading-edge wake, they added a system of discrete, nonintersecting vortex lines to the conventional vortex

lattice employed by Giesing [24] and co-workers. Each line of the system was composed of a series of short straight segments and one (the last) semi-infinite segment. They adjusted the position and orientation of each finite-segment until it was force-free through iteration. These lines then modeled the force-free vortex sheet generated by the leading-edge separation. Subsequently, Kandil [25], and Kandil, Mook, and Nayfeh [26] refined this approach and, for several cases, compared the predicted results with experimental data. They found very close agreement for lift and moment in every case. The approach is not limited by aspect ratio, planform, camber, thickness, or angle of attack as long as separation occurs only along the sharp edges and vortex bursting does not occur near the wing.

Atta [27], and Atta, Kandil, Mook, and Nayfeh [28,29] extended the approach to treat unsteady flows past rectangular wings. Subsequently, Thrasher, Mook, Kandil and Nayfeh [30], and Thrasher [31] refined the approach to treat flows past rectangular wings executing arbitrary maneuvers, while Kandil, Atta and Nayfeh [32], and Atta [33] refined the approach to treat flows past delta wings executing arbitrary maneuvers. Similar approaches were taken, for example, by Belotserkovskii and Nisht [34], Summa [35], and Rebach [36]. Later the general unsteady method was modified

to treat small, harmonic oscillations around an arbitrary constant angle of attack by Nayfeh, Mook and Yen [37]. It was further refined by Konstandinopoulos [38].

Johnson [39] and collaborators developed a vortex-sheet method (or doublet-panel method) which employs rectangular panels of doublets. In this method, the configuration surface is represented by source and/or doublet singularity panels, and the rolled-up vortex sheets and wakes are represented by doublet panels alone. The free sheet and wake are aligned with the local flow. The fed sheet is an entirely kinematic extension of the free sheet and the size of the fed sheet is chosen by experience or from the conical flow results of Smith [16]. The strength of the singularities as well as the shape and position of the free vortex sheets are computed iteratively starting with an assumed initial geometry. During the calculations they encountered convergence problems in many cases and overpredicted the lift coefficients for high aspect ratio wings.

1.3 MOTIVATION FOR THE PRESENT WORK

Although the vortex-lattice technique yields the total loads accurately, it does not always lead to accurate predictions of the pressure distribution unless a very large number of elements is used. However, the increase of the number of elements causes close interaction among the concentrated vortex lines during the iteration procedure which is responsible for the difficulties in achieving convergence in the wake due to the strong algebraic singularity associated with the Biot-Savart law. Also, it requires substantial computational time to achieve acceptable accuracy if the solution converges. As a result, the natural extension and expansion of the vortex lattice technique by replacing the lattice of discrete vortex lines with a continuous distribution of vorticity are needed to improve these shortcomings.

The doublet-panel method projects the actual panel onto the plane defined by the centroid of the four corners and the normal vector obtained from the cross product of the two vectors connectingthe mid-points of opposite sides. (With the present method, triangular panels are used, and hence approximate plane panels are not needed.) Because the doublet distribution is specified over an approximating panel instead of the actual panel, the procedure for

evaluating the velocity field must consider the transfer of the integral from the approximating to the actual surface. (With the present method, such a transfer is not needed.) Moreover, the doublet-panel method has convergence problems in many cases. This difficulty in obtaining convergence is due to the inability to satisfy the continuity of the derivatives of the doublet strength across the edges of adjoining panels. Although Johnson et al. [40] later improved the method by developing a simple least-squares penalty technique to damp the instability that causes the divergence, they were forced to prescribe the orientations of the panels in the fed sheet and the "fixed design wake".

Thus, the desire to accurately predict the aerodynamic characteristics under the conditions of subsonic speeds and high angles of attack with highly swept, low-aspect, delta and delta-like wings and to overcome the drawbacks and disadvantages in the vortex lattice and the doublet panel methods mentioned previously provide the motivation for the present research work. Therefore, a continuous-vorticity panel method has been developed and is presented in detail in Chapter II.

In Chapter II, the basic continuous-vorticity panel method for incompressible flow is introduced to predict the steady aerodynamic loads on lifting surfaces having

sharp-edge separation. Triangular panels with linearly varying vorticity are used. The velocity field generated by an individual element is obtained in closed form and an optimization scheme is constructed for finding the vorticity at the nodes of the elements.

In Chapter III, the panel arrangement for delta wings and the numerical procedure for obtaining the solutions are presented. We also present the computational results and compare them with available experimental data and numerical results for the purpose of examining the validity of this model.

In Chapter IV, we apply the present method to calculate the steady aerodynamic loads on rectangular wings. The panel arrangement and the numerical procedure used to solve this problem are also presented. Computational results are compared with available experimental data and other numerical results for both high-aspect-ratio and low-aspect-ratio rectangular wings.

In Chapter V, some conclusions and recommendations concerning further extensions and modifications of the present method are presented.

Chapter II

FORMULATION OF THE PHYSICAL PHENOMENON

2.1 GENERAL

The problem of airflow around a thin, finite wing which moves in an inviscid, incompressible fluid by using the continuous-vorticity panel method is studied. As the wing, or ideally the lifting surface, moves, it creates a disturbance and sets the air in motion. As a result, vorticity is generated in the boundary layers on the upper and lower sides of the lifting surface. The vortices that form along the sharp edges are shed and convected away from the wing, and constitute the wake. The wing can be simulated by a bound-vortex sheet across which a finite pressure difference exists and hence upon which a force acts. The wake can be simulated by a free-vortex sheet because its position is not specified and the pressure jump across it does not exist.

The total velocity field generated by the vortex sheet must satisfy the continuity equation, which for an incompressible fluid is

$$\nabla \cdot \vec{V} = 0 \qquad (2.1)$$

subject to the following boundary conditions:

1. The disturbance created by the wing must die out with increasing distance away from the wing and its wakes. Hence,

$$|\vec{V}| \to 0 \qquad \text{away from } S_{LS} \text{ and } S_W$$

where S_{LS} denotes the area of the lifting surface and S_W the area of the wake.

2. The fluid particles cannot penetrate the surface of the wing; thus, the normal component of the relative velocity must vanish at the wing surface. That is,

$$(\vec{V} - \vec{V}_{LS}) \cdot \vec{n} = 0 \qquad \text{on } S_{LS}$$

where $\vec{V}$ is the velocity of the fluid particle, $\vec{V}_{LS}$ is the velocity of the lifting surface, and $\vec{n}$ is the unit vector normal to the surface.

In addition to the boundary conditions, several other conditions must also be satisfied:

1. The vorticity field must be divergenceless; hence,

$$\text{div} (\vec{\Omega}) = \text{div} (\text{curl } \vec{V}) \equiv 0.$$

2. The Kutta condition must be satisfied along the sharp leading and trailing edges of the wing. This condition requires that the pressure jump across the lifting surface vanish at the edge.

3. For an inviscid fluid, the Kelvin-Helmholtz theorem requires that all vorticity be transported with the fluid particles. This condition forces a force-free wake and is used to obtain the position of the wake.

2.2 DESCRIPTION OF THE CONTINUOUS-VORTICITY METHOD

This section presents the panel development. The goal is to derive an expression for the induced velocity at an arbitrary point in the space due to an assumed vorticity distribution on the panel.

The first step in panel development is the definition of panel geometry. Kelly [41] examined different shapes for the elements of the lattice on the lifting surface and found that rectangular elements give the best results. Hence, the rectangular element is assumed. Each rectangular element is then divided into four triangular elements. All four corners of a rectangular element do not, in general, lie in the same plane. As a result, the method is not restricted to planar lifting surfaces. For each triangular element, a local rectangular Cartesian coordinate system is introduced such that the x-axis and z-axis lie in the plane of the element. Referring to Fig. 2, the three corners of a typical triangular element are labelled 1, 2, and 3 according to a clockwise convention. The origin of the local reference

frame always coincides with 1. The coordinates of the other two corners are denoted by corresponding subscripts. The velocity field is first calculated in this local reference frame and then transformed into the global reference frame.

Three local, planar, shape functions are introduced and defined as follows:

$$f_1 = a_1 \xi + b_1 \zeta + 1 \tag{2.1a}$$

$$f_2 = a_2 \xi + b_2 \zeta \tag{2.1b}$$

$$f_3 = a_3 \xi + b_3 \zeta \tag{2.1c}$$

where

$$a_1 = (\zeta_3 - \zeta_2)/D, \quad b_1 = (\xi_2 - \xi_3)/D \tag{2.2a}$$

$$a_2 = -\zeta_3/D, \quad b_2 = \xi_3 /D \tag{2.2b}$$

$$a_3 = \zeta_2 /D, \quad b_3 = -\xi_2/D \tag{2.2c}$$

and

$$D = \xi_3 \zeta_2 - \xi_2 \zeta_3 \tag{2.2d}$$

Thus, the function f_1 has the values of unity at 1 and zero at 2 and 3, the function f_2 has the values of unity at 2 and zero at 1 and 3, while the function f_3 has the values of unity at 3 and zero at 1 and 2.

We represent the vorticity of the vortex sheet as follows:

$$\vec{\Omega} = \Omega_x \vec{i} + \Omega_z \vec{k} \tag{2.3a}$$

where

$$\Omega_x = X_1 f_1 + X_2 f_2 + X_3 f_3 \tag{2.3b}$$

$$\Omega_z = Z_1 f_1 + Z_2 f_2 + Z_3 f_3 \tag{2.3c}$$

and the X_n and Z_n are constants, the basic unknowns in the problem. They represent the X-component and Z-component of the vorticity at the corners, or nodes, of the elements.

The X_n and the Z_n are not independent; it follows from

$$\text{div}\ \vec{\Omega} = 0$$

that

$$\sum_{i=1}^{3} a_i X_i = -\sum_{j=1}^{3} b_j Z_j \tag{2.4}$$

We refer to Eq. (2.4) as the conservation equation. The control point for each triangular element is defined to be the centroid of its corners.

2.3 VELOCITY FIELD GENERATED BY VORTICITY DISTRIBUTED OVER A TRIANGULAR PANEL

The velocity generated at an arbitrary point P by the vorticity distributed over one of the elements is given by (e.g., Karamcheti [42])

$$\vec{V} = \frac{1}{4\pi}\,\text{Curl} \iint_{\sigma} \frac{\vec{\Omega}(\vec{s})\,d\sigma}{|\vec{r} - \vec{s}|} \tag{2.5}$$

where σ is the area of the element, $\vec{r} = x\vec{i} + y\vec{j} + z\vec{k}$ is the position vector of point P, and $\vec{s} = \xi\vec{i} + \zeta\vec{k}$ is the position vector of a point in σ. Substituting Eqs. (2.3) into Eq. (2.5), we obtain

$$V = \text{Curl} \sum_{n=1}^{3} (X_n\vec{i} + Z_n\vec{k})B_n(x,y,z) \tag{2.6}$$

where

$$B_n = \frac{1}{4\pi}[a_n I_1 + b_n I_2 + (\delta_{1n} + a_n x + b_n z)I_3] \tag{2.7}$$

$$I_1(x,y,z) = \iint_\sigma \frac{(\xi - x)d\xi d\zeta}{r} \tag{2.8}$$

$$I_2(x,y,z) = \iint_\sigma \frac{(\zeta - z)d\xi d\zeta}{r} \tag{2.9}$$

and

$$I_3(x,y,z) = \iint_\sigma \frac{d\xi d\zeta}{r} \tag{2.10}$$

$$r^2 = (\xi - x)^2 + y^2 + (\zeta - z)^2$$

Substituting Eq. (2.7) into Eq. (2.6), we find

$$V_x = \sum_{n=1}^{3} Z_n \frac{\partial B_n}{\partial y} \tag{2.11}$$

$$V_y = \sum_{n=1}^{3} \left[X_n \frac{\partial B_n}{\partial z} - Z_n \frac{\partial B_n}{\partial x}\right] \tag{2.12}$$

$$V_z = -\sum_{n=1}^{3} X_n \frac{\partial B_n}{\partial y} \tag{2.13}$$

It follows from Eq. (2.7) that in order to obtain the three partial derivatives of the B_n, we need the following ten quantities:

$$\frac{\partial I_1}{\partial x}, \quad \frac{\partial I_1}{\partial y}, \quad \frac{\partial I_1}{\partial z}, \quad \frac{\partial I_2}{\partial x}, \quad \frac{\partial I_2}{\partial y}, \quad \frac{\partial I_2}{\partial z}, \quad \frac{\partial I_3}{\partial x}, \quad \frac{\partial I_3}{\partial y}, \quad \frac{\partial I_3}{\partial z}, \text{ and } I_3$$

In the next three paragraphs the expressions for these ten quantities are developed.

Referring to Fig. 3, we can write

$$I_1 = \int_0^c \int_{\frac{b\zeta}{c}}^{\frac{b-a}{c}\zeta+a} \frac{(\xi - x)d\xi d\zeta}{r} = \int_0^c [(a - x + \frac{b-a}{c}\zeta)^2 + y^2 + (\zeta - z)^2]^{1/2} d\zeta - \int_0^c [(\frac{b\zeta}{c} - x)^2 + y^2 + (\zeta - z)^2]^{1/2} d\zeta \tag{2.14}$$

Differentiating Eq. (2.14) and then integrating the results, we obtain the following

$$\frac{\partial I_1}{\partial x} = (x - a)H_1 + (\frac{a-b}{c})H_2 - xH_3 + \frac{b}{c} H_4 \tag{2.15}$$

$$\frac{\partial I_1}{\partial y} = y(H_1 - H_3) \tag{2.16}$$

$$\frac{\partial I_1}{\partial z} = H_4 - H_2 + z(H_1 - H_3) \tag{2.17}$$

where

$$H_1 = \int_0^c [(a - x + \frac{b-a}{c}\zeta)^2 + y^2 + (\zeta - z)^2]^{-1/2} d\zeta = \frac{1}{\sqrt{\alpha_{11}}} \ln\left(\frac{c\alpha_{11} - \alpha_{12} + \sqrt{\alpha_{11}}\, r_2}{\sqrt{\alpha_{11}}\, r_1 - \alpha_{12}}\right) \tag{2.18}$$

$$H_2 = \int_0^c [(a - x + \frac{b-a}{c}\zeta)^2 + y^2 + (\zeta - z)^2]^{-1/2} \zeta d\zeta = \frac{r_2 - r_1}{\alpha_{11}} + \frac{\alpha_{12}}{\alpha_{11}} H_1 \tag{2.19}$$

$$H_3 = \int_0^c [(\frac{b\zeta}{c} - x)^2 + y^2 + (\zeta - z)^2]^{-1/2}\, d\zeta$$

$$= \frac{1}{\sqrt{\alpha_{21}}} \ln\left(\frac{c\alpha_{21} - \alpha_{22} + \sqrt{\alpha_{21}}\, r_2}{\sqrt{\alpha_{21}}\, r_1 - \alpha_{22}}\right) \tag{2.20}$$

$$H_4 = \int_0^c [(\frac{b\zeta}{c} - x)^2 + y^2 + (\zeta - z)^2]^{-1/2}\, \zeta d\zeta \tag{2.21}$$

$$= \frac{r_2 - r_1}{\alpha_{21}} + \frac{\alpha_{22}}{\alpha_{21}} H_3$$

$$r_1 = (x^2 + y^2 + z^2)^{1/2} \tag{2.22}$$

$$r_2 = [(b - x)^2 + y^2 + (c - z)^2]^{1/2} \tag{2.23}$$

$$r_3 = [(a - x)^2 + y^2 + z^2]^{1/2} \tag{2.24}$$

$$\alpha_{11} = 1 + \frac{(b - a)^2}{c^2}, \quad \alpha_{12} = z - \frac{(b - a)(a - x)}{c} \tag{2.25}$$

$$\alpha_{21} = 1 + \frac{b^2}{c^2}, \quad \alpha_{22} = z + \frac{bx}{c}$$

Again referring to Fig. 3, we can write

$$I_2 = \int_0^b \int_0^{\frac{c\xi}{a}} \frac{(\zeta - z)d\zeta d\xi}{r}$$

$$+ \int_b^a \int_0^{\frac{(\xi - a)c}{b - a}} \frac{(\zeta - z)d\zeta d\xi}{r} \tag{2.26}$$

Integrating once, then differentiating the results, and finally integrating a second time, we obtain

$$\frac{\partial I_2}{\partial x} = -F_2 + xF_1 + r_3 - r_1 - F_5 + xF_4 \tag{2.27}$$

$$\frac{\partial I_2}{\partial y} = y(F_1 - F_3 + F_4) \tag{2.28}$$

$$\frac{\partial I_2}{\partial z} = zF_1 - \frac{c}{b} F_2 - zF_3 + (\frac{ac}{b - a} + z)F_4 + \frac{c}{a - b} F_5 \tag{2.29}$$

where

$$F_1 = \int_0^b [(\xi - x)^2 + y^2 + (\frac{c\xi}{b} - z)^2]^{-1/2}\, d\xi$$

$$= \frac{1}{\sqrt{\beta_{11}}} \ln\left(\frac{b\beta_{11} - \beta_{12} + \sqrt{\beta_{11}}\, r_2}{\sqrt{\beta_{11}}\, r_1 - \beta_{12}}\right) \tag{2.30}$$

$$F_2 = \int_0^b [(\xi - x)^2 + y^2 + (\frac{c\xi}{b} - z)^2]^{-1/2}\, \xi d\xi$$

$$= \frac{r_2 - r_1}{\beta_{11}} + \frac{\beta_{12}}{\beta_{11}} F_1 \tag{2.31}$$

$$F_3 = \int_0^a [(\xi - x)^2 + y^2 + z^2]^{-1/2}\, d\xi = \ln \frac{a - x + r_1}{r_1 - x} \tag{2.32}$$

$$F_4 = \int_b^a [(\xi - x)^2 + y^2 + (\frac{\xi - a}{b - a} c - z)^2]^{-1/2}\, d\xi$$

$$= \frac{1}{\sqrt{\beta_{21}}} \ln \frac{a\beta_{21} - \beta_{22} + \sqrt{\beta_{21}}\, r_1}{b\beta_{21} - \beta_{22} + \sqrt{\beta_{21}}\, r_2} \tag{2.33}$$

$$F_5 = \int_b^a [(\xi - x)^2 + y^2 + (\frac{\xi - a}{b - a} c - z)^2]^{-1/2}\, \xi d\xi$$

$$= \frac{r_1 - r_2}{\beta_{21}} + \frac{\beta_{22}}{\beta_{21}} F_4 \tag{2.34}$$

$$\beta_{11} = 1 + \frac{c^2}{b^2}, \quad \beta_{12} = x + \frac{cz}{b} \quad \beta_{21} = 1 + \frac{c^2}{(b - a)^2}, \tag{2.35}$$

$$\beta_{22} = x + (z + \frac{ac}{b - a}) \frac{c}{b - a}$$

To develop I_3 and its derivatives, we follow Hess and Smith [43]. They show that

$$I_3 = h_{12}Q_{12} + h_{23}Q_{23} + h_{31}Q_{31} + |y| (J_{12} + J_{23} + J_{31} - |y|\Delta\theta) \tag{2.36}$$

where

$$Q_{ij} = \ln\left(\frac{r_i + r_j + d_{ij}}{r_i + r_j - d_{ij}}\right) \tag{2.37}$$

$$J_{ij} = \tan^{-1}\left[\frac{h_{ij}|y|(r_i \ell_{ij}^{(2)} - r_j \ell_{ij}^{(1)})}{r_i r_j h_{ij}^2 + y^2 \ell_{ij}^{(1)} \ell_{ij}^{(2)}}\right] \tag{2.38}$$

The quantities r_i are defined in Eqs. (2.22)-(2.24). The remaining quantities (d_{ij} , h_{ij} , $\ell_{ij}^{(1)}$, and $\ell_{ij}^{(2)}$) are defined in terms of the coordinates of the nodal points of the triangular area ($\xi_1 = \zeta_1 = 0$; $\xi_2 = b$ and $\zeta_2 = c$, and $\xi_3 = a$ and $\zeta_3 = 0$):

$$\ell_{ij}^{(1)} = (\xi_i - x)C_{ij} + (\zeta_i - z)S_{ij} \tag{2.39}$$

$$\ell_{ij}^{(2)} = (\xi_j - x)C_{ij} + (\zeta_j - z)S_{ij} \tag{2.40}$$

$$C_{ij} = \frac{\xi_j - \xi_i}{d_{ij}} \tag{2.41}$$

$$S_{ij} = \frac{\zeta_j - \zeta_i}{d_{ij}} \tag{2.42}$$

$$d_{ij} = \sqrt{(\xi_j - \xi_i)^2 + (\zeta_j - \zeta_i)^2} \tag{2.43}$$

$$h_{ij} = (x - \xi_i)S_{ij} - (z - \zeta_i)C_{ij} \tag{2.44}$$

Finally,

$$\Delta\theta = \begin{cases} 2\pi & \text{if the projection of P onto the plane of the triangle lies inside } \sigma \\ 0 & \text{otherwise} \end{cases} \tag{2.45}$$

It can be shown [43] that

$$\frac{\partial I_1}{\partial x} = S_{12}Q_{12} + S_{23}Q_{23} + S_{31}Q_{31} \tag{2.46}$$

$$\frac{\partial I_3}{\partial y} = -\mathrm{sgn}(y)(\Delta\theta - J_{12} - J_{23} - J_{31}) \tag{2.47}$$

$$\frac{\partial I_3}{\partial z} = -C_{12}Q_{12} - C_{23}Q_{23} - C_{31}Q_{31} \tag{2.48}$$

One example of a closed-form expression for the velocity generated at an arbitrary point P by the vorticity distributed over a triangular panel is given in Appendix C.

2.4 VORTEX CORES AND SEMI-INFINITE PANELS

In addition to the triangular panels described in Section 2.2, vortex cores and semi-infinite panels have been used to represent more realistically the physics of the vortex formation. In this section, we describe these and develop expressions for the velocity fields they generate.

A. Vortex Cores

In Fig. 4 we represent a flat sheet of linearly varying vorticity, being fed by a straight vortex core along its edge. $\Gamma(x)$ is the variable circulation around the core and $\gamma(x)$ is the continuously varying product of the vorticity and the thickness of the sheet. Since vorticity is a divergenceless field, we have

$$\oint\!\!\!\oint_{\sigma} \vec{\Omega} \cdot \vec{n}\, d\sigma = 0 \tag{2.49}$$

where σ is a simple closed surface, $\vec{\Omega}$ is the vorticity, and $\vec{n}$ is a unit vector normal to σ. Applying Eq. (2.49) to an infinitesimal length of core in Fig. 4, we obtain

$$\frac{d\Gamma}{dx} = -\gamma(x) \tag{2.50}$$

In the present application, $\gamma(x)$ is always linear; thus, γ has the form

$$-\gamma = Ax + B \tag{2.51}$$

where A and B are constants. It follows that

$$\Gamma = \frac{1}{2} Ax^2 + Bx + C \tag{2.52}$$

where C is the constant of integration.

Referring to Fig. 5, we note that the velocity generated at point P by the action of the vortex core alone is [42]

$$\vec{v} = \frac{\vec{e}}{4\pi h} \int_{\theta_1}^{\theta_2} \Gamma \sin\theta \, d\theta \tag{2.53}$$

where

$$\vec{e} = \frac{\vec{\omega} \times \vec{r}_1}{|\vec{\omega} \times \vec{r}_1|}$$

and $\vec{\omega}$ is a vector parallel to the vortex core.

Substituting Eq. (2.52) into Eq. (2.53) yields

$$\vec{v} = \frac{\vec{e}}{4\pi h} \int_{\theta_1}^{\theta_2} \left(\frac{1}{2} Ax^2 + Bx + C\right) \sin\theta \, d\theta \tag{2.54}$$

x can be represented as a function of θ:

$$x = \bar{x} - h\cot\theta \tag{2.55}$$

After substituting Eq. (2.55) into Eq. (2.54) and integrating, we obtain

$$\vec{V} = \frac{\vec{e}}{4\pi h}\left\{\frac{1}{2}Ar_1^2\left[\cos 2\theta_1(\cos\theta_1 - \cos\theta_2) + \sin 2\theta_1(\sin\theta_1 - \sin\theta_2) + \frac{1}{2}(1 - \cos 2\theta_1)\ln\left(\frac{(1 - \cos\theta_2)\sin\theta_1}{(1 - \cos\theta_1)\sin\theta_2}\right)\right] + Br_1[1 - \cos(\theta_1 - \theta_2)] + C(\cos\theta_1 - \cos\theta_2)\right\} \tag{2.56}$$

B. Semi-Infinite Panels

Here we consider semi-infinite panels in which the vorticity varies linearly and is parallel to the length. The situation is represented in Fig. 6. We develop expressions for the derivatives of the Bn by considering the limit as the coordinate a in Fig. 3 approaches infinity.

It follows from Eq. (2.2) that as $a \to \infty$

$$a_n \to 0 \qquad \text{for all } n \tag{2.57}$$

and

$$b_1 \to -\frac{1}{c}, \quad b_2 \to \frac{1}{c}, \quad \text{and} \quad b_3 \to 0 \tag{2.58}$$

and hence from Eq. (2.7) that

$$B_n \to \frac{1}{4\pi}[b_n I_2 + (\delta_{1n} + b_n z) I_3] \tag{2.59}$$

In order to develop expressions for the derivatives of the B_n, the following seven quantities are needed:

$$\frac{\partial I_2}{\partial x}, \quad \frac{\partial I_2}{\partial y}, \quad \frac{\partial I_2}{\partial z}, \quad \frac{\partial I_3}{\partial x}, \quad \frac{\partial I_3}{\partial y}, \quad \frac{\partial I_3}{\partial z}, \quad I_3$$

The expressions for the limits of these quantities are developed next.

It follows from Eq. (2.22)-(2.24) that as a increases, r_1 and r_2 remain unchanged and

$$r_3 \to a - x + \ldots \tag{2.60}$$

(We note that a is always positive.) From Eq. (2.35) we find that β_{11} and β_{12} remain unchanged while

$$\beta_{21} \to 1 \qquad \text{and} \qquad \beta_{22} \to x \tag{2.61}$$

Hence F_1 and F_2 remain unchanged while

$$F_3 \to \ell n\left(\frac{2a}{r_1 - x}\right) \tag{2.62}$$

$$F_4 \to \ell n\left(\frac{2a}{b - x + r_2}\right) \tag{2.63}$$

$$F_5 \to a - x + x\ell n\left(\frac{2a}{b - x + r_2}\right) \tag{2.64}$$

Substituting Eqs. (2.62)-(2.64) into Eqs. (2.27)-(2.29) yields

$$\frac{\partial I_2}{\partial x} = xF_1 - F_2 - r_1 \tag{2.65}$$

$$\frac{\partial I_2}{\partial y} = y[F_1 + \ell n(\frac{r_1 - x}{b + r_2 - x})] \tag{2.66}$$

$$\frac{\partial I_2}{\partial z} = c + zF_1 - \frac{c}{b} F_2 + z\ell n(r_1 - x) \tag{2.67}$$

$$- (z - c)\ell n(b + r_2 - x) - c\ell n(2a)$$

It follows from Eqs. (2.37) and (2.38) that Q_{12} and J_{12} remain unchanged while

$$J_{23} \to \tan^{-1}[\frac{(z - c)|y|(b - x - r_2)}{r_2(z - c)^2 + y^2(b - x)}] \tag{2.68}$$

$$J_{31} \to \tan^{-1}[\frac{z|y|(r_1 + x)}{r_1 z^2 - y^2 x}] \tag{2.69}$$

$$Q_{23} \to \ell n(\frac{2a}{r_2 + b - x}) \tag{2.70}$$

$$Q_{31} \to \ell n(\frac{2a}{r_1 - x}) \tag{2.71}$$

Substituting Eqs. (2.68)-(2.71) into Eqs. (2.46)-(2.48), we obtain

$$\frac{\partial I_1}{\partial x} \to S_{12}Q_{12} \tag{2.72}$$

$$\frac{\partial I_1}{\partial y} \to -sgn(y)(\Delta\theta - J_{12} - J_{23} - J_{31}) \tag{2.73}$$

$$\frac{\partial I_1}{\partial z} \to -C_{12}Q_{12} + \ell n(\frac{r_2 + b - x}{r_1 - x}) \tag{2.74}$$

And from Eq. (2.36) we obtain

$$I_3 \to h_{12}Q_{12} + (z - c)\ell n(r_2 + b - x) \tag{2.75}$$

$$- z\ell n(r_1 - x) + c\ell n(2a)$$

$$+ |y|(J_{12} + J_{23} + J_{31} - \Delta\theta)$$

Differentiating Eq. (2.59) and then substituting Eqs. (2.65)-(2.67) and (2.72)-(2.74) into the results, we find that

$$\lim_{a\to\infty}\left(\frac{\partial B_n}{\partial x}\right) = \frac{1}{4\pi}\left[b_n(xF_1 - F_2 r_2 - r_1)\right.$$

$$\left. + (\delta_{1n} + b_n z)S_{12}Q_{12}\right] \tag{2.76}$$

$$\lim_{a\to\infty}\left(\frac{\partial B_n}{\partial y}\right) = \frac{1}{4\pi}\left\{b_n y\left[F_1 + \ln\left(\frac{r_1 - x}{b + r_2 - x}\right)\right]\right.$$

$$\left. - \operatorname{sgn}(y)(\delta_{1n} + b_n z)(\Delta\theta - J_{12} - J_{23} - J_{31})\right\} \tag{2.77}$$

$$\lim_{a\to\infty}\left(\frac{\partial B_n}{\partial z}\right) = \frac{1}{4\pi}\left\{b_n\left[c + zF_1 - \frac{c}{b}F_2 + h_{12}Q_{12}\right.\right. \tag{2.78}$$

$$\left. + |y|(J_{12} + J_{23} + J_{31} - \Delta\theta)\right]$$

$$\left. + (\delta_{1n} + b_n z)\left[\ln\left(\frac{r_2 + b - x}{r_1 - x}\right) - C_{12}Q_{12}\right]\right\}$$

2.5 DETERMINATION OF THE VORTICITY

After knowing how to obtain the induced velocities in terms of the closed-form expressions mentioned above, we are ready to find the values of the vorticity components at the corners of the triangular elements by satisfying the no-penetration boundary condition, the conservation condition Eq. (2.4), and the Kutta condition simultaneously.

Ideally, the component of the velocity normal to the lifting surface should vanish everywhere on the surface. But this is impossible with a finite number of triangles to

satisfy other conditions. In fact, it is impossible to satisfy the no-penetration condition at all the control points simultaneously. Thus, we resort to a scheme that finds the vorticity distribution corresponding to a minimum of some measure of the flow through the lifting surface and satisfying the conservation and Kutta conditions as constraints.

We begin by calculating a set of influence coefficients that provides the normal components of the velocities at the control points of triangular elements on the lifting surface generated by the shape functions of all the triangular panels, semi-infinite panels, and the concentrated vortex cores. Using these coefficients, we can set up an influence coefficient matrix A, for the vector of unknown components of the vorticity U, such that A, U, the vector of contributions from the free stream V, and the vector of normal components of the velocity E at the control points are related by

$$AU + V = E \tag{2.79}$$

The vector E may be interpreted as a deviation vector from the no-penetration boundary condition. This is discussed in detail in Appendix A.

The present scheme determines U such that the square of a weighted magnitude of E is a minimum, subject to the constraints imposed by the conservation and Kutta conditions. To obtain the quantity that is to be minimized, we pre-multiply both sides of Eq. (2.79) by the product of the transpose of E and a symmetric weighting matrix, W:

$$U^TA^TWAU + U^TA^TWV + V^TWAU + V^TWV = E^TWE$$

Since each term is a scalar, each term equals its own transpose. We have

$$U^TA^TWAU + 2V^TWAU + V^TWV = E^TWE = \phi \tag{2.80}$$

Then the method of Lagrange multipliers is used to form the augmented function Φ_A:

$$\Phi_A = \phi + \lambda_C^TCU + \lambda_K^TKU \tag{2.81}$$

where λ_C and λ_K are the vectors of Lagrange multipliers, and the matrices C and K are used to express the conservation condition

$$CU = 0 \tag{2.82}$$

(see also Eq. (2.4)) and the Kutta condition

$$KU = 0 \tag{2.83}$$

For the Kutta condition, we require the pressure jump across the lifting surface to vanish at the edge. It then follows that the vorticity and velocity fields should be parallel along the edge. To impose this condition of parallel fields requires an iteration in addition to that required to locate the wake. However, from the experimentally determined vorticity fields of Hummel [5], and Francis and Kennedy [6], and Elle and Jones [3], it appears that the vortex lines are orthogonal to the edges where the Kutta condition is imposed, i.e., to the edges where wakes are attached. Thus, we require the vortex lines to be orthogonal to these edges.

The details of the present optimization scheme are given in Appendix B.

Then the vectors U, λ_C and λ_K are found by solving the following simultaneous algebraic equations

$$\nabla_U \Phi_A = 2(A^T W A)U + 2A^T W V + C^T \lambda_C + K^T \lambda_k = 0 \qquad (2.84)$$

and Eqs. (2.82) and (2.83). After these equations have been solved, we can calculate the pressure distribution and the resultant loads.

2.6 CALCULATION OF LOADS

After the vorticity at the nodes and the shape of the wake have been obtained, the loads are calculated. To calculate the loads, we first need to find the velocity generated at the control point by the free stream and all the panels of vorticity; this is labelled $\vec{V}$. The jump in the tangential velocity across the vortex sheet is given by

$$\Delta\vec{V} = \vec{n} \times \vec{\Omega} \tag{2.85}$$

where $\vec{n}$ is the unit vector normal to the surface. Thus, on the upper side of the element,

$$\vec{V}_u = \vec{V} + \frac{1}{2}\Delta\vec{V} \tag{2.86a}$$

while on the lower side

$$\vec{V}_l = \vec{V} - \frac{1}{2}\Delta\vec{V} \tag{2.86b}$$

Here we are concerned with a uniform stream, having the speed U_∞, passing over the lifting surface. Then, from Bernoulli's equation, it follows that, at the control point, the pressures on the upper and lower surfaces are given by

$$P_u = P_\infty + \frac{\rho}{2}(U_\infty^2 - V_u^2) \tag{2.87a}$$

and

$$P_l = P_\infty + \frac{\rho}{2}(U_\infty^2 - V_l^2) \tag{2.87b}$$

The nondimensional pressure jump across the lifting surface is given by

$$\Delta C_p = \frac{p_\ell - p_u}{\frac{1}{2}\rho U_\infty^2} = \frac{V_u^2 - V_\ell^2}{U_\infty^2} \tag{2.88}$$

Substituting Eqs. (2.86) into Eq. (2.88) leads to

$$\Delta C_p = 2\vec{V} \cdot \Delta\vec{V}/U_\infty^2 \tag{2.89}$$

After the pressure is calculated, the force on the triangular element is obtained by multiplying the pressure jump at the control point by the area. Then the lift force and the pitching moment can be calculated.

Chapter III

DELTA WINGS

3.1 PANEL ARRANGEMENT

A lattice of lines is placed on a delta wing as indicated in Fig. 7. This lattice is the same one used in the uniform-element, discrete-vortex technique. Then each rectangular element is divided into four triangular panels. Also, the leading-edge vortex sheet is modeled by first forming a lattice of lines as in the general discrete vortex-lattice method, and then dividing each quadrilateral element into two triangular panels, as shown in Fig. 7. The vorticity is perpendicular to the leading edge due to the Kutta condition and varies linearly across each element. For example, in Fig. 7, the vorticity is perpendicular to line AB and varies linearly from point A to point B. In the wake, the vorticity varies linearly (between the same two values) from point A' to point B', etc. Moreover, the vorticity in triangle A'A''B' is parallel to line A'A'' which in turn is aligned with the vorticity at the centroid of triangle A'A''B'. At the end of each row of finite-length elements in each wake line, we add a semi-infinite panel

with the vorticity aligned parallel to the free-stream velocity. Because the wake rolls up tightly at high angles of attack, a concentrated vortex core is also used to represent the leading-edge vortex core.

3.2 NUMERICAL PROCEDURE

The boundary-value problem of Chapter II is nonlinear because the shapes of the separated vortex sheets as well as the vorticity distributions over the wing surface and wakes are unknown. Therefore, an iterative method is required. Initially, we guess the coordinates of the end points of the short, straight segments in the lines representing the free-vortex sheets. Then we form the lattice by connecting the ends of adjacent segments in different lines, and from the lattice we form the triangular panels. The influence coefficients of the induced velocity at each control point are calculated for all the triangular panels, semi-infinite panels, and the concentrated vortex core by using the closed-form expressions of Chapter II. Then the values of the vorticity components at the corners of the triangular panels on the wing surface and in the wake are determined by minimizing the square of a weighted magnitude of the deviation vector E from the no-penetration boundary condition, subject to the constraints imposed by the

conservation and Kutta conditions. The satisfaction of the conservation equation in the shaded triangular panels, as shown in Fig. 7, forces its satisfaction in the unshaded panels also. The solution of the set of simultaneous algebraic equations yields the vorticity distribution.

Next, with the known vorticity distribution, we calculate the velocity at the centroids of each of the triangular elements in the leading row of the wake. Then we align the edges of the triangles that form the borders of the leading row with the velocities at the centroids of the same triangles. In the remaining rows of elements in the wake, we calculate the velocity at the centroids at every other triangular element, starting with the second element in each row. Then we align the edges of the triangles that form the rearward boarder of the row with the velocities at the centroids of the same triangles. Thus the shape and the orientation of the triangular panels representing the wake are changed. Also, at high angles of attack the wake rolls up tightly so that we employ a concentrated core of vorticity to simulate the leading-edge-vortex core and its feeding sheet. The procedure for adding a concentrated vortex core is summarized below

First, we specify the X-components of the positions of the end points of each of the finite-length segment in the

first and second wake lines emanating from the leading edge. Then we compare the Z-components of the positions of the points in the first wake line with those of the points having the same X-components of positions in the second wake line. As the wake rolls up tightly, the second wake line may cross the first wake line. If this happens, the Z-component of the position of point A will be larger than that of point B, which are shown in Fig. 8. Then we make the panels on the right-hand side of the line AC collapse into a discrete core. In fact, the line AC and the semi-infinite line CD is the leading-edge vortex core being fed by the remaining vortex panels in the wake.

After we relocate the wake, one iterative cycle is accomplished. Then we redetermine the vorticity field on the wing and in the wake; and then we relocate the wake. Several iterative cycles are performed until the shape of the wake converges. After the vorticity at the nodes and the shape of the wake have been obtained, the total loads and pressure distributions can be calculated by using Bernoulli's equation. The details of all the calculations required above are given in Chapter II.

3.3 NUMERICAL RESULTS

In Fig. 9, we compare the vorticity field observed by Elle and Jones [3] with that computed by the present method for a delta wing of 1.87 aspect ratio. The present results were computed for 15° angle of attack. The precise value of the angle of attack for the observation of Elle and Jones was not given; they simply stated that it was high incidence. We note that the observed vorticity is nearly perpendicular to the leading edge, so we use this requirement as the Kutta condition for the present model. The two vorticity fields appear to be consistent.

In Fig. 10, the actual solution of the positions of the finite segments in the wake for a delta wing of unit aspect ratio for 10° angle of attack is shown in two views. The converged solution shows the leading-edge core and its feeding free-vortex sheets. As the angle of attack increases, the vortex sheet rolls up more tightly. In Fig. 11, the actual solution for the same delta wing is shown for 15° angle of attack. Here we can see that the first and second wake lines emanating from the leading edge cross each other earlier than those for 10° angle of attack. Semi-infinite segments and panels are also used.

Each component in the deviation vector E measures the degree of the inaccuracy in satisfying the no-penetration

boundary condition at the corresponding control point. The ratio of the magnitude of the maximum component in the vector E to the free stream speed is denoted by δ. Numerical examples are given for a delta wing of 1.46 aspect ratio. The values of δ are 0.148, 0.159, and 0.195 for the angles of attack of 10°, 15°, and 20°, respectively. The maximum component in the vector E always corresponds to the control point nearest the apex. Our numerical experience shows that putting a small weight on the corresponding element in the symmetric weighting matrix W not only reduces this maximum deviation (i.e. spreads the errors all over the control points on the wing surface more evenly) but also increases the convergence. As a matter of fact, however, these small deviations do not significantly influence the calculated loads in the present method as seen in Eq. (2.89) because $\Delta\vec{V}$ is the tangential velocity on the wing surface and hence the dot product of $\vec{V}$ and $\Delta\vec{V}$ eliminates the Y-component of $\vec{V}$.

In Fig. 12, the normal-force coefficient is given as a function of the angle of attack for a delta wing of unit aspect ratio. The numerical results obtained by the present method are compared with the experimental values of Peckham [2] and Tosti [44], and the numerical results of Kandil et al [26], Weber et al [45], Mehrotra and Lan [46], and Lamar and Gloss [47] over a range from 0° to 20°. There is fairly

good agreement among the present results, all of the experimental data, and the other numerical results. The effect of increasing the number of rows for the present method is also shown in this figure. One can see that the curves based on the lattices having three rows and four rows are almost coincident. In Figs. 13-15, the same coefficients are given as functions of the angle of attack for delta wings having various aspect ratios. For 1.46 aspect ratio, the normal-force coefficients predicted by the present method compare well with the data of Wentz and Kohlman [48] and the numerical results of Mehrotra and Lan [46], Lamar and Gloss [47], and Weber et al [45] in the angle of attack range from 0° to 20°. For 1.67 aspect ratio, the present results for normal-force coefficient agree closely with the experimental data of Peckham [2] and Bergesen and Porter [49] and numerical results of Kandil et al [26], as shown in Fig. 14. The agreement of the present results for 2.0 aspect ratio with the experimental data of Bartlett and Vidal [50] and numerical results of Kandil et al [26] is also good, as shown in Fig. 15.

In Figs. 16-17, we show the variation of the theoretical normal-force coefficient for delta wings with aspect ratio at fixed angles of attack of 15° and 20°, respectively. The results predicted by the present method are compared with

the suction analogy [47] which is known to be a good estimator of the actual normal-force coefficient. Good agreement between the present method and the suction analogy occurs in the range of aspect ratios of $1.0 < A < 2.0$.

The pitching-moment coefficient for a flat delta wing of unit aspect ratio is shown in Fig. 18. The results obtained by the present method agree closely with the experimental data of Peckham [2] and Tosti [44] and the numerical results of Weber et al [45] and Mehrotra and Lan [46]. In Fig. 19, we compare the pitching-moment coefficient for a flat delta wing of 1.46 aspect ratio predicted by the present method with other numerical results and with experimental data. The agreement of our results with those of Weber et al [45] and Mehrotra and Lan [46] is quite good. The agreement of our results with the experimental data presented by Wentz and Kohlman [48] is very good for angles of attack lower than 15°.

One of the most important features of the present method is the ability to compute surface pressure distributions. A comparison of detailed pressure distributions are shown in Figs. 20, 21 and 22. In Fig. 20, the spanwise pressure distributions for a flat delta wing of aspect ratio 1.46 at 14° angle of attack are compared with the experimental data of Marsden et al [17] and numerical results of Mehrotra and

Lan [46], and Weber et al [45] at two chordwise stations. The general agreement of our results with the experimental data is quite good. The present method predicts the completely three-dimensional non-conical load distribution very well including the location of the pressure peak induced by the vortex core. We also compare spanwise pressure distributions predicted by the present method based on two criteria for the formation of the vortex core. One can see that the tight criterion (Appendix D) gives the results in closer agreement with the experimentally obtained values as shown in Fig. 20. So the vortex core should be modeled more realistically by using the tight criterion. This can be seen in Fig. 24 which shows the actual solution of the positions of the finite segments in the wake for a delta wing of 1.46 aspect ratio for a 14° angle of attack. Fig. 21 compares the spanwise pressure distributions predicted by the present method with other numerical results for a flat delta wing of unit aspect ratio at 15° angle of attack. The results are in good agreement at $X/C_r = 0.7$ and $X/C_r = 0.82$, except the peak values of ΔC_p given by the numerical results of Weber et al [45] seem to be higher. The spanwise pressure distributions predicted by the pesent method, shown in Fig. 22, on an aspect ratio 1.0 delta wing at an angle of. attack of 20° are compared with the

experimental data of Hummel [5]. The agreement of the present results with the experimental data is good. The decrease of the load toward the trailing edge is predicted well.

Chapter IV

RECTANGULAR WINGS

4.1 PANEL ARRANGEMENT

A. High-Aspect Rectangular Wings

We divide a typical rectangular wing into m rows and n columns, that is, (m-1)(n-1) rectangular elements. Each rectangular element is then divided into four triangular panels, as shown in Fig. 25. For a high-aspect wing, the wing-tip vortices appear not to influence strongly a significant percentage of the surface of the wing. Hence, along the wing tips and the leading edge a concentrated core of vorticity is employed to simulate the wing-tip vortex and the flow around a small radius leading edge. Vorticity enters and leaves this core at all points along the wing tips and leading edge, but not in the wake. The vorticity along the trailing edge is taken to be perpendicular to the edge as the Kutta condition. The free vortex sheet emanating from the trailing edge is represented by a flat sheet which is composed of a series of connected triangular panels, as shown in Fig. 25. This flat sheet is aligned with the velocity of the free stream.

B. Low-Aspect Rectangular Wings

The same lattice of lines is placed on the wing surface as the one for high-aspect ratios. For low-aspect wings, the wing-tip vortices play an important role in the nonlinear effects predicting the aerodynamic characteristics. Therefore, the Kutta condition imposed along the wing tips requires that the vorticity be perpendicular to the wing tips and vary linearly from point A to point B. The wake emanating from the wing tips is represented by a series of triangular panels whose orientation in space is determined as part of the solution, as shown in Fig. 25. Semi-infinite panels are added to the end of each row of finite-length elements in each wake line. For the rectangular wing of unit aspect ratio at 15° angle of attack, the first two wake lines emanating from the wing tips do not cross each other until they pass the trailing edge. Therefore, we don't employ a concentrated core of vorticity to represent the wing-tip vortex core which appears to form behind the trailing edge and not to have much influence on the aerodynamic loads.

4.2 NUMERICAL PROCEDURE

For high-aspect wings, the boundary-value problem can be treated as a linear, two-dimensional problem. Hence, no iteration is needed to adjust the wake shape. The only unknowns are the vorticity distributions over the surface of the wing. The solution can be obtained by first forming an influence matrix in which the influence coefficients of the induced velocity at each control point are calculated for all the triangular panels and semi-infinite panels. Also, the conservation equation being satisfied in the shaded triangular panels forces the conservation equation to be satisfied in the unshaded panels, as shown in Fig. 25. Then we apply the same optimization scheme as in the case of the delta wing to minimize the errors from the no-penetration boundary condition with Kutta and conservation equations as the constraints. This involves the setting up of a coefficient matrix and selecting a solver for the simultaneous algebraic equations. Then the vorticity distributions over the lifting surface for high aspect ratios can be obtained.

For low-aspect wings, we need to determine the wake shape emanating from the wing tips in addition to the vorticity distributions over the wing surface. The numerical procedure for obtaining these solutions is similar to the

one used to treat delta wings, except no concentrated core of vorticity is added to the wake lines emanating from the wing tips.

4.3 NUMERICAL RESULTS

In Fig. 26, we show the vorticity fields simulating rectangular wings of different high-aspect ratios. The arrows point in the direction of the vorticity and their lengths are proportional to the magnitude. We note that the vorticity along the trailing edge is weak everywhere except in a small region near the tips. The vorticity fields depicted are actual solutions obtained by using eight rectangular elements. Symmetry was not imposed a priori; thus, the program can treat asymmetric flows. The vorticity fields are qualitatively consistent with the observations of Francis and Kennedy [6], except near the midspan where their experimental observations were influenced by the wall of the tunnel.

In Fig. 27, the normal-force coefficient is given as a function of the aspect ratio for a 15° angle of attack. The present results agree closely with experimental data when the aspect ratio is larger than 3. Below this value, it appears that the wing tip vortices strongly influence a significant percentage of the surface of the wing and a

better model of the wing tip vortices for low-aspect ratio is then needed.

Fig. 28 shows the wake shape in two views for a rectangular wing of unit aspect ratio in symmetric steady flow at a 15° angle of attack. Symmetry was not imposed a priori; thus, the program can treat asymmetric flows. This figure is similar to those obtained by Belotserkovskii [22] and Rehbach [51].

In Fig. 29, the normal force coefficient is given as a function of the angle of attack. The present results are in good agreement with the numerical results of Bradley et al [53] and with the experimental data of Ermolenko [52] and Lamar [54]. The differences in experimental data can be attributed to the different construction of the wing tip.

In Fig. 30, the pitching-moment coefficient is given as a function of the angle of attack. The agreement is good between the predictions given by the present method and the experimental data of Ermolenko [52].

In Fig. 31, the normal-force coefficient is given as a function of aspect ratio for a low-aspect rectangular wing at 15° angle of attack. The present results agree closely with the experimental data of Lamar [54] and numerical results of Kandil [25]. Combining Fig. 27 with Fig. 31, the whole range of the normal-force coefficient given as a function of the aspect ratio can be displayed.

Fig. 32 shows the vorticity fields simulating the rectangular wing of unit aspect ratio. In order to include the significant influence of the wing-tip vortices on the surface of the wing, the Kutta condition for the present method has been employed so that the vorticity is perpendicular to the wing tips and the trailing edge. The arrows indicate the direction of the vorticity and their lengths are proportional to the magnitude.

Chapter V

CONCLUSIONS AND RECOMMENDATIONS

A continuous-vorticity panel method that can predict the steady aerodynamic loads on lifting surfaces has been developed. The method is based on the assumption that vortex bursting does not occur in the vicinity of the wing and separation occurs only along sharp edges. The method employs an inviscid-flow model in which the wing and the wake are replaced by triangular panels and semi-infinite panels with linearly varying vorticity. If the wake rolls up tightly, vortex cores are modeled by the present method.

For moderate and high angles of attack, for small aspect ratios, and for highly swept sharp leading edges, This method which models the wakes with force-free continuous vortex sheets has succeeded in predicting the distributed as well as the total aerodynamic characteristics. The present method is not restricted by aspect ratio, angle of attack, planform, or camber. Moreover, for a delta wing, the present method can model the leading-edge vortex core and its feeding sheet. For a rectangular wing of high aspect ratio, a concentrated core of vorticity along the wing tips and the leading edge can provide an accurate model.

The present method predicts vorticity fields for rectangular and delta wings which are qualitatively consistent with experimental results. The normal-force and pitching-moment coefficients are in good agreement with experimentally obtained values. Moreover, the present method is capable of predicting the detailed surface pressure distributions on thin, sharp-edged wings better than the vortex-lattice methods. The results show good agreement with available experimental data.

The method is general, and it can treat lifting and nonlifting flows. It can be used to predict loads on any control surface, including diving planes and sails on submarines.

The following are areas for improving and extending the present method:

1. Discretizing the continuous time variation to treat unsteady flows. At each discrete time step, the solution is obtained in a manner similar to that for treating steady flows.
2. Generalizing the present code to handle planforms other than the delta and rectangular planforms.
3. Including the thickness and camber effects.
4. Taking into account the compressibility effects by using a Prandtl-Glauert transformation based on freestream or local conditions.

5. Combining the present code with a boundary-layer program to predict separation, transition, etc.
6. Combining the present code with a stress and/or deflection code to calculate the deformation of wings under aerodynamic loads.

REFERENCES

1. Maskell, E. C., "Some Recent Developments in the Study of Edge Vortices," Proceedings of 3rd Congress of Int. Counc. Aero. Sci., 737-749, 1962, Sportan Books, Inc. Washington, 1964.

2. Peckham, D. H., "Low-Speed Wind-Tunnel Tests on a Series of Uncambered Slender Pointed Wings with Sharp Edges," RM 3186, British Aeronautical Research Council, 1961.

3. Elle, B. J. and Jones, J. P., "A Note on the Vorticity Distribution on the Surface of Slender Delta Wings with Leading Edge Separation," J. of Royal Aero. Soc. 65, 195-198, 1961

4. Mangler, K. W. and Smith, J. H. B., "Calculation of the Flow Past Slender Delta Wings with Leading Edge Separation," RAE Report Aero. 2593, May, 1957.

5. Hummel, D., "On the Vortex Formation Over a Slender Wing at Large Angles of Incidences," AGARD CP-247, January 1979.

6. Francis, M. S. and Kennedy, D. A., "Formation of a Trailing Vortex," J. of Aircraft, 3, 148-154, 1979.

7. Prandtl, L., "Tragflugeltheorie," Nachr. Ges. Wiss. Gottingen, 107-451, 1918.

8. Ashley, H. and Rodden, W. P., "Wing-Body Aerodynamic Interaction," Annual Review of Fluid Mechanics, Vol. 4, 431-472, 1972.

9. Belotserkovskii, S. M., "Study of the Unsteady Aerodynamics of Lifting Surfaces Using the Computer," Annual Review of Fluid Mechanics, Vol. 9, 469-494, 1977.

10. Bollay, W., "A Non-Linear Wing Theory and its Application to Rectangular Wings of Small Aspect Ratio," ZAMM 19, 21-35, 1939.

11. Gersten, K., "Nichtlineare Tragflachentheorie, insbesondere fur Flugel mit Bleinem Seitenverhaltnis," Ing. Archiv 30, 431-452, 1961.

12. Polhamus, E. C., "A Concept of the Vortex Lift of Sharp-Edged Delta Wings based on a Leading-Edge-Suction Analogy," NASA TN-D 3767, 1966.

13. Legendre, R., "Ecoulement an voisinage de la pointe avant d'une aile a forte fleche aux incidences moyennes," 8eme Congr. Int. Mec. App. Istanbul, 1952, Rech. Aero. 30, 1952, et 31, 1953.

14. Brown, C. E. and Michael, W. H., "Effect of Leading-Edge Separation on the Lift of a Delta Wing," J. of Aero. Soc. 21, 690-694, 1954 and 706, NACA TN 3430, 1955.

15. Mangler, K. W. and Smith, J. H. B., "A Theory of the Flow Past a Slender Delta Wing with Leading-Edge Separation," Proc. Royal. Soc. Lond. A 251, 200-217, 1959.

16. Smith, J. H. B., "Improved Calculations of Leading-Edge Separation from Slender Delta Wings," Proc. Royal. Soc. Lond. A 306, 1968, RAE Tech. Report 66070, 1966.

17. Marsden, D. J., Simpson, R. W. and Rainbird, W. J., "The Flow over Delta Wings at Low Speeds with Leading-Edge Separation," College of Aeronautics, Cranfield, Report 114, 1958.

18. Hummel, D., "Zur Umstromung Scharfkantiger Schlanker Deltaflugel bei grosen Anstellwinkeln," Z. Flugwiss. 15, 376-385, 1967.

19. Hummel, D. and Redeker, G., "Experimentelle Bestimmung der gebundenen Wirbellinien sowie des Stromungsverlaufs in der Umgebung der Hinterkante eines schlanken Deltaflugels," Abhandlg. d. Braunschw. Wiss. Ges. 22, 273-290, 1972.

20. Nangia, R. K. and Hancock, G. J., "A Theoretical Investigation for Delta Wings with Leading-Edge Separation at Low Speeds," ARC CP 1086, 1968.

21. Matoi, T. K., Covert. E. E. and Widnall, S. E., "A Three-Dimensional Lifting-Surface Theory with Leading-Edge Vortices," ONR-CR-215-230-2, 1975.

22. Belotserkovskii, S. M., "Calculation of the Flow around Wings of Arbitrary Planforms in a wide Range of Angles of Attack," NASA TT F-12, 291, 1969.

23. Mook, D. T. and Maddox, S. A., "Extension of a Vortex-Lattice Method to Include the Effects of Leading-Edge Separation," J. of Aircraft, 11, 127-128, 1974.

24. Giesing, J. P., Kalman, T. P. and Rodden, W. P., "A Subsonic Unsteady Aerodynamics for General Configurations," AIAA Paper No. 72-76, 1972.

25. Kandil, O. A., "Prediction of the Steady Aerodynamic Loads on Lifting Surfaces Having Sharp-Edge Separation," Ph.D. Dissertation, Engineering Science and Mechanics Dept., Virginia Polytechnic Institute and State University, December 1974.

26. Kandil, O. A., Mook, D. T. and Nayfeh, A. H., "Nonlinear Prediction of the Aerodynamic Loads on Lifting Surfaces," AIAA Paper No. 74-503, 1974.

27. Atta, E. H., "Unsteady Flow over Arbitrary Wing-Planforms Including Tip Separation," M.S. Thesis, Dept. of Engineering Science and Mechanics, Virginia Polytechnic Institute and State University, Blacksburg, Virginia, 1976.

28. Atta, E. H., Kandil, O. A., Mook, D. T. and Nayfeh, A. H., "Unsteady Flow Past Wings Having Sharp-Edge Separation," NASA SP-405, 407-418, 1976.

29. Atta, E. H., Kandil, O. A., Mook, D. T. and Nayfeh, A. H., "Unsteady Aerodynamic Loads on Arbitrary Wings Including Wing-Tip and Leading-Edge Separation," AIAA Paper No. 77-156, 1977.

30. Thrasher, D. F., Mook, D. T., Kandil, O. A. and Nayfeh, A. H., "Application of the Vortex-Lattice Concept to General, Unsteady Lifting-Surface Problems," AIAA Paper No. 77-1157, 1977.

31. Thrasher, D. F., "Nonlinear Unsteady Aerodynamics with Application to Dynamic-Aerodynamic Interaction," M.S. Thesis, Dept. of Engineering Science and Mechanics, Virginia Polytechnic Institute and State University, Blacksburg, Virginia, May 1979.

32. Kandil, O. A., Atta, E. H. and Nayfeh, A. H., "Three Dimensional Steady and Unsteady Asymmetric Flow Past Wings of Arbitrary Planforms," AGARD Paper No. 2, AGARD Fluid Dynamics Panel Symposium, Unsteady Aerodynamics, Ottawa, Canada, 1977.

33. Atta, E. H., "Nonlinear Steady and Unsteady Aerodynamics of Wings and Wing-Body Combinations," Ph.D. Dissertation, Dept. of Engineering Science and Mechanics, Virginia Polytechnic Institute and State University, Blacksburg, Virginia, May 1978.

34. Belotserkovskii, S. M. and Nisht, M. I., "Nonstationary Nonlinear Theory of a Thin Wing of Arbitrary Planform," Fluid Dynamics, Vol. 9, No. 4, 583-598, 1974.

35. Summa, J. M., "Potential Flow about Three-Dimensional Lifting Configurations with Applications to Wings and Rotors," AIAA Paper No. 75-126, 1975.

36. Rehbach, C., "Numerical Investigation of Leading-Edge Vortex for Low-Aspect-Ratio Thin Wings," AIAA J., Vol. 14, No. 2, February 1976.

37. Nayfeh, A. H., Mook, D. T. and Yen, A., "The Aerodynamics of Small Harmonic Oscillations around Large Angles of Attack," AIAA Paper No. 79-1520, 1979.

38. Konstadinopoulos, P., "A Vortex-Lattice Method for General, Unsteady, Subsonic Aerodynamics," M.S. Thesis, Dept. of Engineering Science and Mechanics, Virginia Polytechnic Institute and State University, July 1981.

39. Johnson, F. T., Lu, P., Brune, G. W., Weber, J. A. and Rubbert, P. E., "An Improved Method for the Prediction of Completely Three-Dimensional Aerodynamic Load Distributions of Configurations with Leading-Edge Vortex Separation," AIAA Paper No. 76-417, 1976.

40. Johnson, F. T., Tinoco, E. N., Lu, P. and Epton, M. A., "Recent Advances in the Solution of Three-Dimensional Flows over Wings with Leading Edge Vortex Separation," AIAA Paper No. 79-0282, 1979.

41. Kelly, S. G., "A Systematic Investigation of the Parameters Affecting the Accuracy of the Vortex-Lattice Method," M.S. Thesis, Dept. of Engineering Science and Mechanics, Virginia Polytechnic Institute and State University, Blacksburg, Virginia, May 1977.

42. Karamcheti, K., Principles of Ideal-Fluid Aerodynamics, Wiley-Interscience, New York, 1966, Chap. 18.

43. Hess, J. L. and Smith, A. M. O., "Calculation of Potential Flow About Arbitrary Bodies," Progress in Aeronau-

tical Sciences, Vol. 8, Pergamon Press, New York, 1-138, 1966.

44. Tosti, L. P., "Low-Speed Static Stability and Damping-in-Roll Characteristics of Some Swept and Unswept Low-Aspect Ratio Wings," NACA TN 1468, 1974.

45. Weber, J. A., Brune, G. W., Johnson, F. T., Lu, P. and Rubbert, P. E., "A Three-Dimensional Solution of Flows over Wings with Leading-Edge Vortex Separation," AIAA Paper No. 75-866, June 1975.

46. Mehrotra, S. C. and Lan, E. E., "A Theoretical Investigation of the Aerodynamics of Low Aspect Ratio Wings with Partial Leading-Edge Separation," NASA CR-145304, 1978.

47. Lamar, J. E. and Gloss, B. B., "Subsonic Aerodynamic Characteristics of Interacting Lifting Surfaces with Separated Flow Around Sharp Edges Predicted by a Vortex-Lattice Method," NASA TN D-7921, 1975.

48. Wentz, W. H. Jr. and Kohlman, D. L., "Wind-Tunnel Investigation of Vortex Breakdown on Slender Sharp-Edged Wings," NASA CR-98737, 1968.

49. Bergesen, A. J. and Porter, J. D., "An Investigation of the Flow Around Slender Delta Wings with Leading-Edge Separation," Report No. 510, Princeton University, Dept. of Aeronautical Engineering.

50. Bartlett, G. E. and Vidal, R. J., "Experimental Investigation of Influence of Edge Shape on the Aerodynamic Characteristics of Low Aspect Ratio Wings at Low Speeds," J. of Aeronautical Sciences, 22(8), 517-533.

51. Rehbach, C., "Calculation of Flows Around Zero-Thickness Wings with Evolute Vortex Sheets," TT F-15, 183, 1973, NASA.

52. Ermolenko, S. D., "Nonlinear Theory of Small Aspect Ratio Wings," Soviet Aeronautics 9, 5-11, 1966.

53. Bradley, R. G., Smith, C. W. and Bhateley, I. C., "Vortex-Lift Prediction for Complex Wing Planforms," J. of Aircraft, 10, 379-381, 1973.

54. Lamar, J. E., "Extension of Leading-Edge Suction Analogy to Wings with Separated Flow Around the Side Edges at Subsonic Speeds," NASA TR R-428, 1974.

55. Winter, H., "Flow Phenomena on Plates and Airfoils of Short Span," NACA Rept. 798, 1937.

Appendix A

INFLUENCE COEFFICIENTS

The induced velocity generated by the vorticity distributed over a triangular panel or a semi-infinite panel has been derived in Chapter II and can be expressed as a linear function of the basic unknowns X_n and Z_n, the X-component and Z-component of the vorticity at the corners of the panels in the local reference frame. Thus, referring to Eqs. (2.11)-(2.13), we have

$$V_x = \sum_{n=1}^{3} Z_n B_{ny} \tag{A.1}$$

$$V_y = \sum_{n=1}^{3} [X_n B_{nz} - Z_n B_{nx}] \tag{A.2}$$

$$V_z = - \sum_{n=1}^{3} X_n B_{ny} \tag{A.3}$$

where $B_{nx}=\frac{\partial B_n}{\partial x}$, $B_{ny}=\frac{\partial B_n}{\partial y}$, and $B_{nz}=\frac{\partial B_n}{\partial z}$. Then the velocity is transformed into the global reference frame

$$V_X = V_x e_{xX} + V_y e_{yX} + V_z e_{zX} \tag{A.4}$$

$$V_Y = V_x e_{xY} + V_y e_{yY} + V_z e_{zY} \tag{A.5}$$

$$V_Z = V_x e_{xZ} + V_y e_{yZ} + V_z e_{zZ} \tag{A.6}$$

where e_{xX} , e_{yX} , e_{zX} , e_{xY} , e_{yY} , e_{zY} , e_{xZ} , e_{yZ} , and e_{zZ} represent the direction cosines of the x, y, and z axes in the global coordinate system (X, Y, Z system). In a similar way, the vorticity components X_n and Z_n at the corners of the panels in the local coordinate system can be transformed into the expressions in terms of the vorticity components X_{ng} and Z_{ng} at the corresponding corners of the panels in the global coordinate system.

Therefore, the normal component of the induced velocity at the control pbint on the lifting surface in the global reference frame can be represented by a linear function of the vorticity components X_{ng} and Z_{ng} at the corners of the panels. That is

$$V_Y = \sum_{n=1}^{3} (X_{ng}C_{nx} + Z_{ng}C_{nz}) \qquad (A.7)$$

where C_{nX} and C_{nZ} can be calculated and are known values.

Then application of the no-penetration boundary condition at all the control points on the lifting surface leads to a set of simultaneous algebraic equations whose matrix form can be written as

$$AU + V = E$$

where A is called the influence coefficient matrix, U is a vector which is composed of the unknowns X_{ng} and Z_{ng}

representing the vorticity components at the nodes of the panels, V is the vector of contributions from the freestream velocity, and E is a deviation vector from the no-penetration boundary condition.

Appendix B

OPTIMIZATION SCHEME

To minimize the error in the no-penetration boundary codition subject to the conservation and Kutta conditions as the constraints, we first obtain the matrix forms of these conditions and then apply the method of Lagrange multipliers. The unknowns X_{ng}, Z_{ng}, and the Lagrange multipliers are obtained by solving a set of simultaneous algebraic equations.

We can rewrite Eq. (2.4), which is known as the conservation equation, as a linear function of the vorticity components X_{ng} and Z_{ng} at the nodes of the panels in a global reference frame by using the same transformation technique as that in Appendix A. The matrix form of the conservation condition is

$$CU = 0$$

where C may be interpreted as the conservation coefficient matrix.

The Kutta condition is taken into account when we form the influence coefficient matrix A; that is, the vortex lines are required to be orthogonal to the edges where the

Kutta condition is imposed, to the edges where wakes are attached. Therefore, along these edges the orientation of the vorticity at a node is known so that only one unknown at this node is counted rather than two.

Then the augmented function Φ_A (Eq.(2.81)) and Eq. (2.84) are reduced to

$$\Phi_A = \Phi + \lambda_C^T C\, U \tag{B.1}$$

and

$$\nabla_U \Phi_A = 2(A^T W A)U + 2A^T W V + C^T \lambda_C = 0 \tag{B.2}$$

To find the vectors U and λ_C, we need to solve the combined simultaneous algebraic equations (B.2) and (2.82). The matrix form of these combined simultaneous algebraic equations is

$$\begin{bmatrix} 2A^T W A & C^T \\ C & 0 \end{bmatrix} \begin{bmatrix} U \\ \lambda_C \end{bmatrix} = \begin{bmatrix} -2A^T W V \\ 0 \end{bmatrix} \tag{B.3}$$

Appendix C

A CLOSED-FORM EXPRESSION FOR THE VELOCITY GENERATED BY THE VORTICITY DISTRIBUTED OVER A TRIANGULAR PANEL

Here we take the X-component of the induced velocity as our example and show how its closed-form expression is obtained.

Referring to Eq. (2.11), we have

$$V_x = Z_1 \frac{\partial B_1}{\partial y} + Z_2 \frac{\partial B_2}{\partial y} + Z_3 \frac{\partial B_3}{\partial y} \tag{C.1}$$

Substituting Eq. (2.7) into Eq. (C.1) gives

$$V_x = \frac{1}{4\pi}\left\{\left(\sum_{n=1}^{3} a_n Z_n\right)\frac{\partial I_1}{\partial y} + \left(\sum_{n=1}^{3} b_n Z_n\right)\frac{\partial I_2}{\partial y} + \left[Z_1 + \sum_{n=1}^{3} (a_n x + b_n z) Z_n\right]\frac{\partial I_3}{\partial y}\right\} \tag{C.2}$$

Then substituting Eqs. (2.16), (2.28), and (2.47) into Eq. (C.2), we obtain

$$V_x = \frac{1}{4\pi}\left\{y\left[\left(\sum_{n=1}^{3} a_n Z_n\right)(H_1 - H_3) + \left(\sum_{n=1}^{3} b_n Z_n\right)(F_1 - F_3 + F_4)\right] - \operatorname{sgn}(y)(\Delta\theta - J_{12} - J_{23} - J_{31})\left[Z_1 + \sum_{n=1}^{3} (a_n x + b_n z) Z_n\right]\right\} \tag{C.3}$$

Appendix D

TIGHT CRITERION FOR THE FORMATION OF THE VORTEX CORE

In section 3.2 we have described the procedure of adding a concentrated vortex core into the wake by comparing the Z-components of the positions of the end points of each finite-length segment in the first wake line with those in the second wake line. In addition to the comparisons mentioned above, the tight criterion requires more comparisons for the Z-components of the positions of the end points of each finite-length segment in all the wake lines emanating from the leading edge.

Referring to Fig. 23, for example, the points A in the first wake line, C in the second wake line, and E in the third wake line have the same X-components as the points B in the second wake line, D in the third wake line, and F in the fourth wake line, respectively. Then their Z-components are compared. As the wake rolls up tightly, the second wake line will cross the first and the third wake line will cross the second and so forth. Therefore, the Z-components of the positions of points A, C, and E are larger than those of points B, D, and F, respectively. If this situation happens, the panels on the right-hand side of the zigzag line AG are

merged into a discrete vortex core. This criterion is more strict than the previous criterion described in section 3.2. The tight criterion gives better distributed aerodynamic loads, though the total aerodynamic loads obtained by both criterions are almost the same.

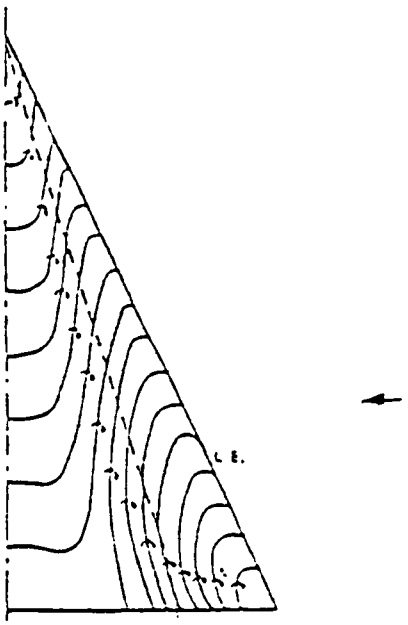

Figure 1: Vortex patterns in the surface of a delta wing at high angles of attack from Elle and Jones [3].

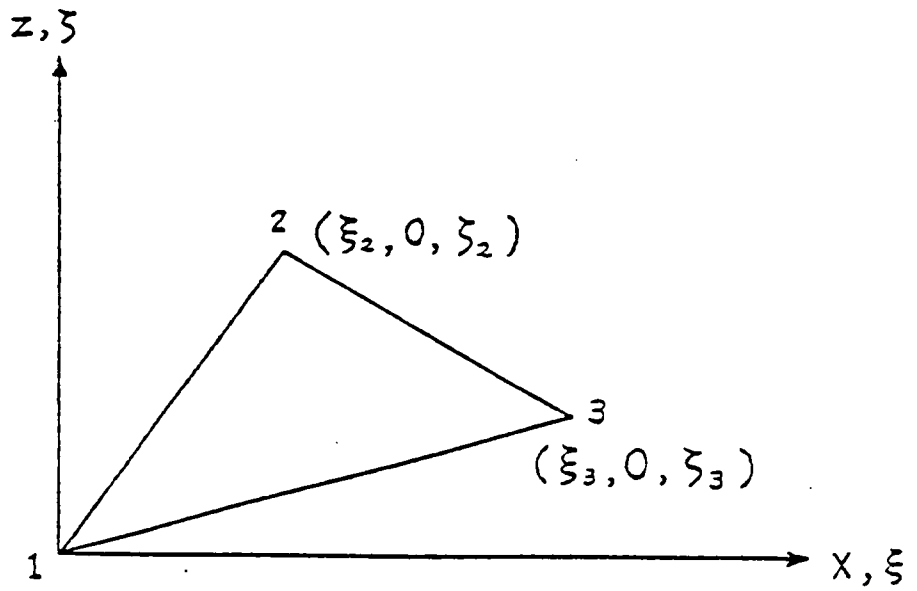

Figure 2: Typical triangular element.

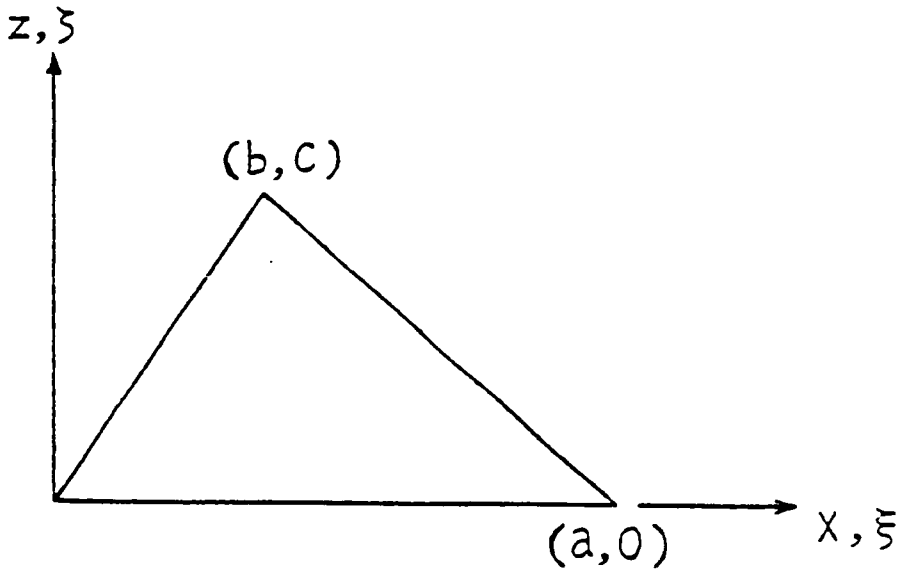

Figure 3: Element used for evaluating integrals.

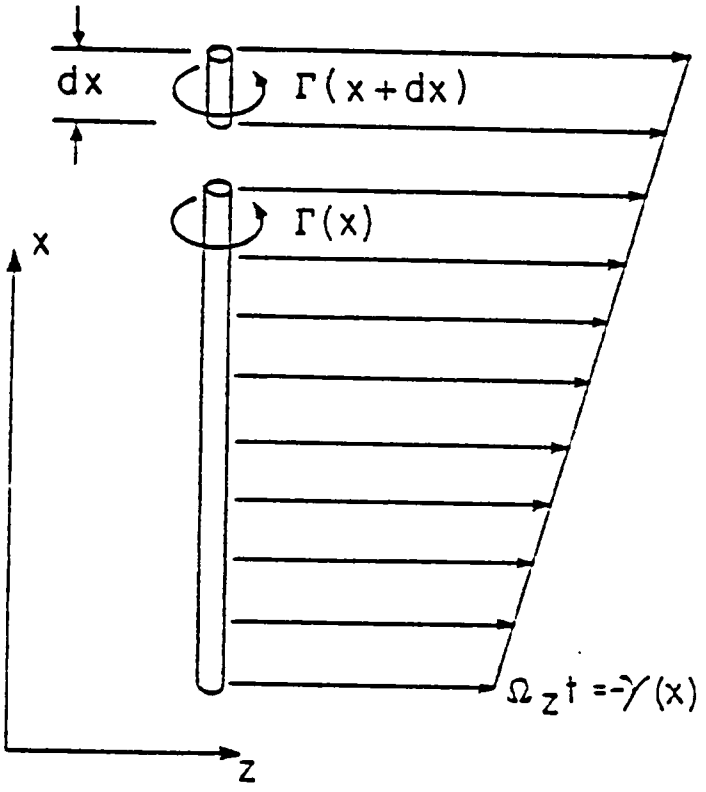

Figure 4: Vortex core and attached vortex sheet.

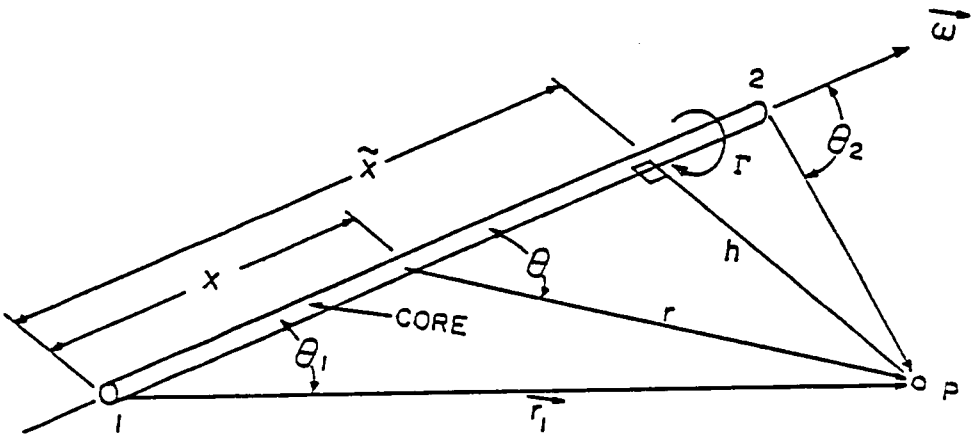

Figure 5: Vortex core and field point P where the velocity is being determined.

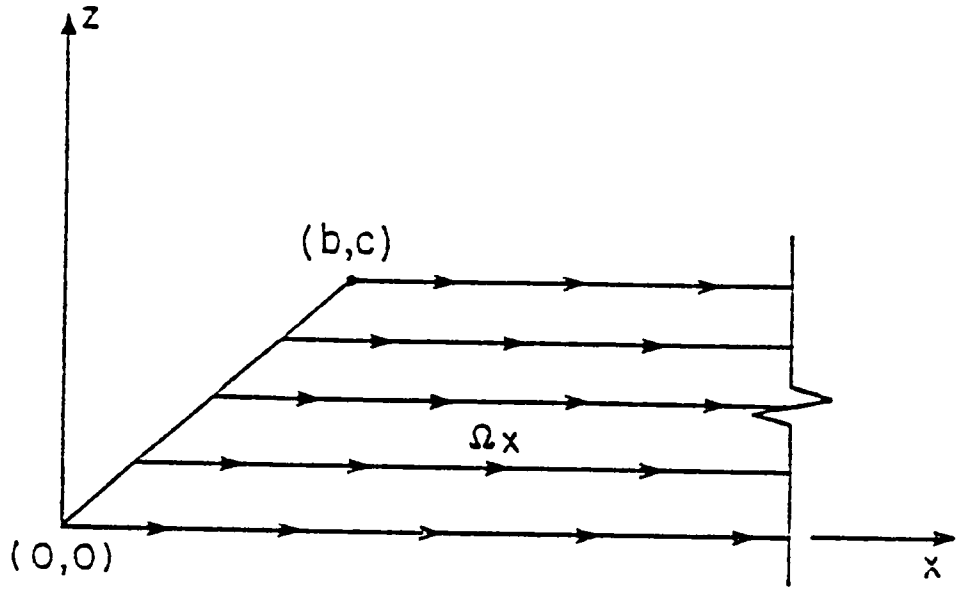

Figure 6: Semi-infinite panel.

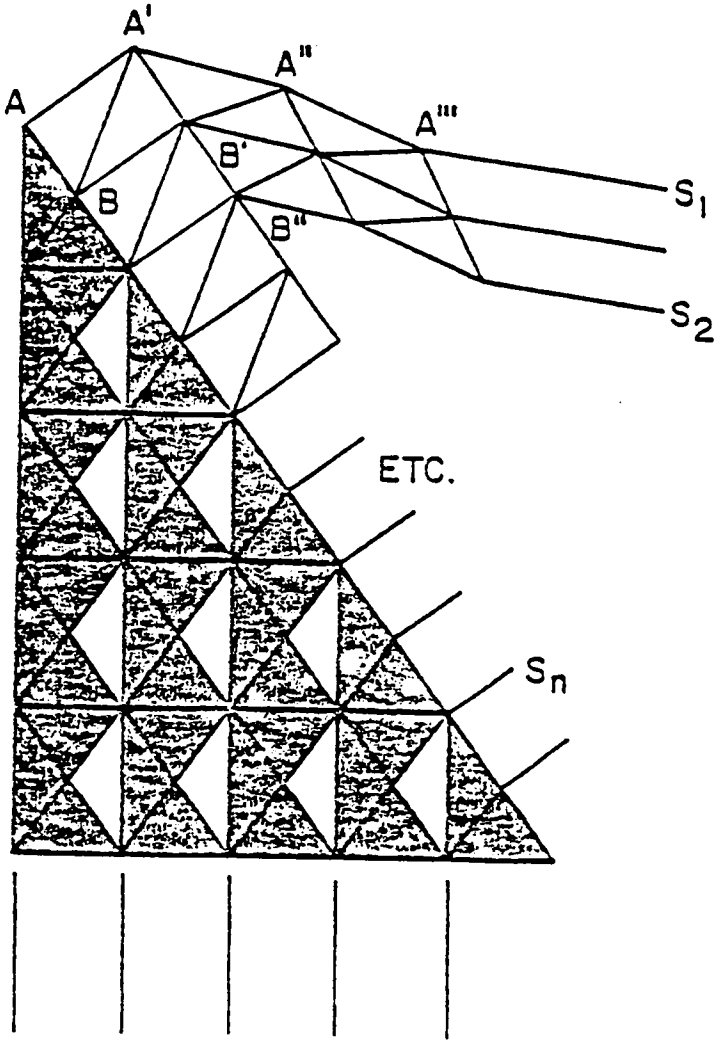

Figure 7: The arrangement of the panels for a delta wing.

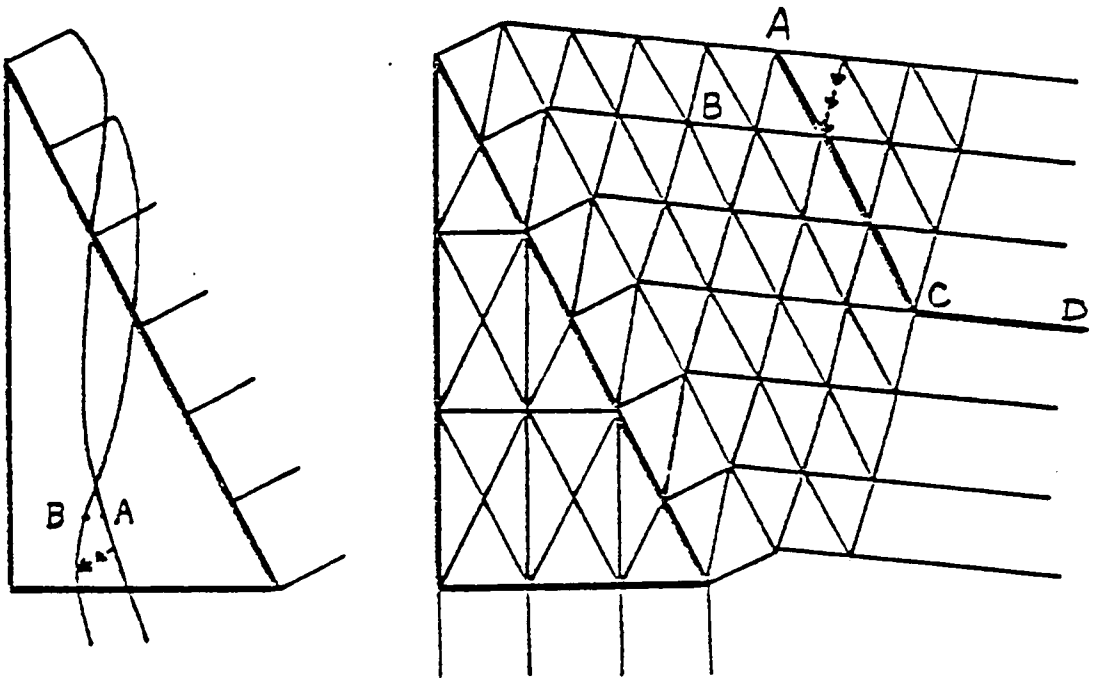

Figure 8: The arrangement of the vortex core.

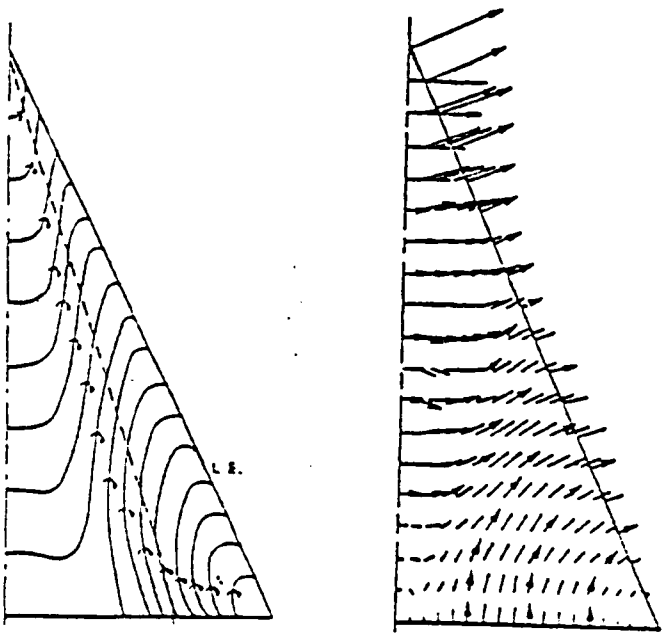

(a)

Experimental results
of Elle and Jones [3]

(b)

Results predicted
by the present method

Figure 9: Comparison of experimental and predicted vorticity fields for a delta wing of 1.87 aspect ratio.

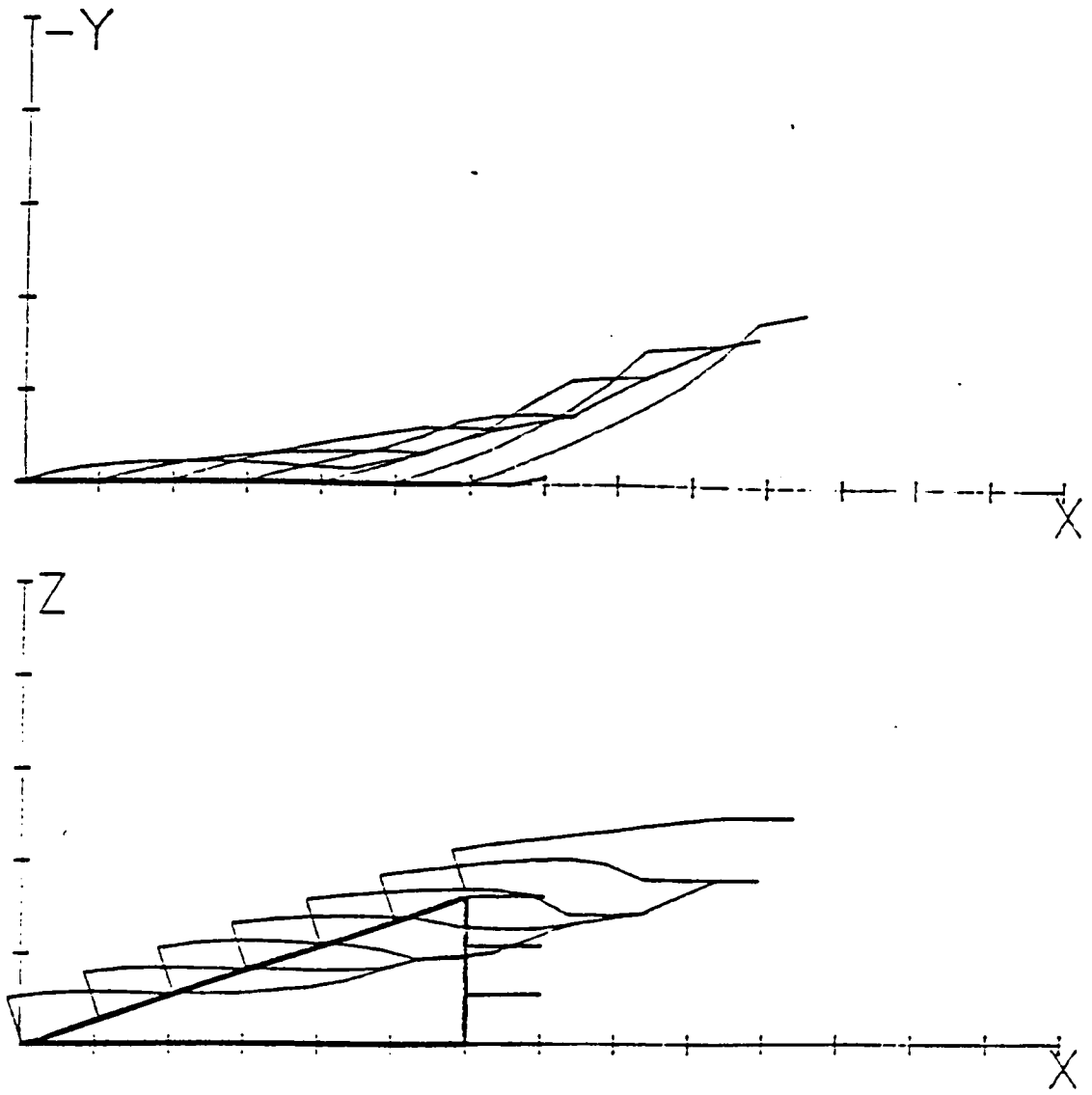

Figure 10: Solution for a delta wing by using loose criterion for the vortex core: AR=1, 10° angle of attack.

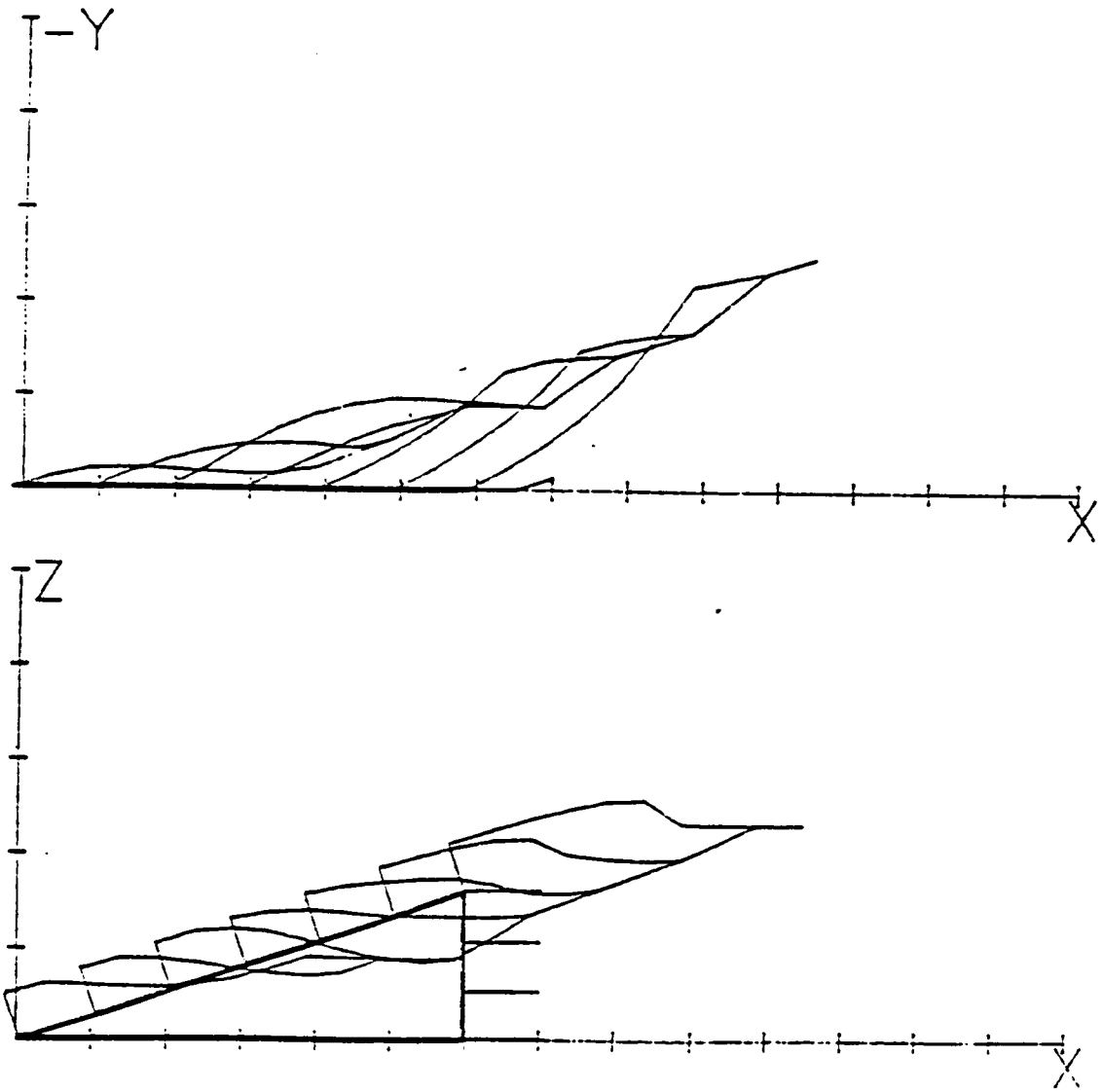

Figure 11: Solution for a delta wing by using loose criterion for the vortex core: AR=1, 15° angle of attack.

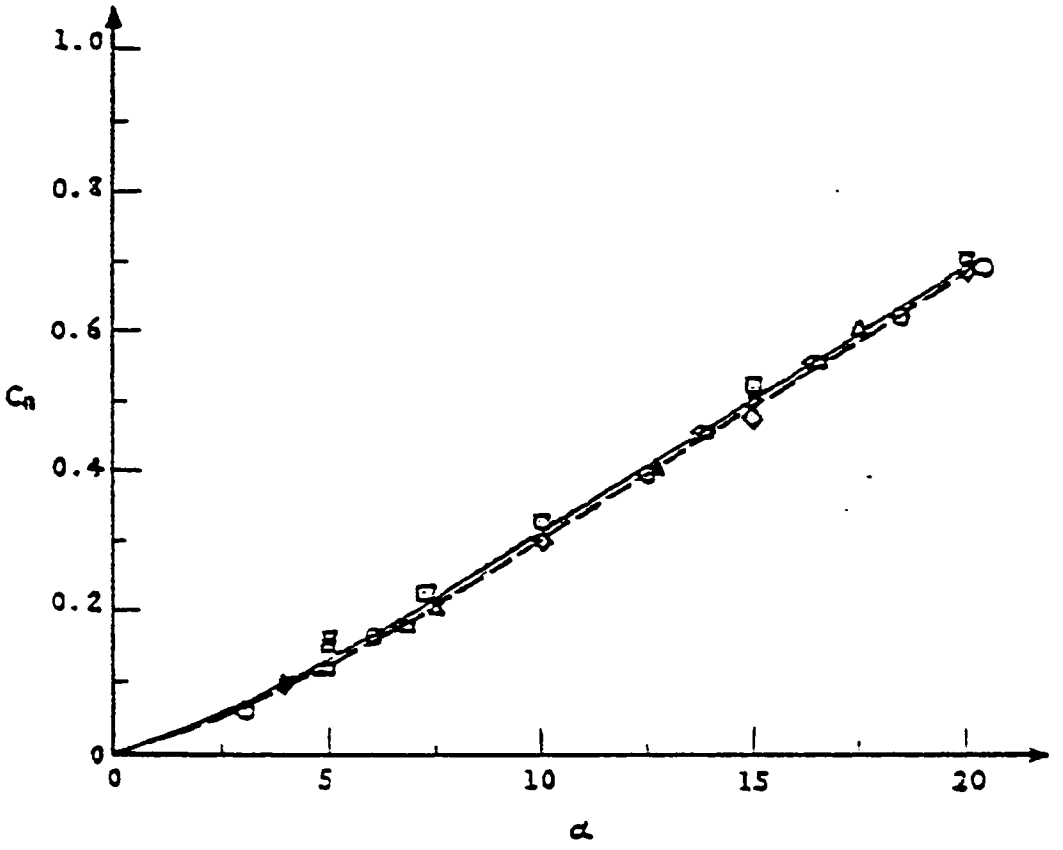

Numerical Results

- Kandil et al [26]
- Weber et al [45]
- Mehrotra and Lan [46]
- Lamar and Gloss [47]
- ——— (3 rows) } Present method
- — — — (4 rows) }

Experimental Results

- Peckham [2]
- Tosti [44]

Figure 12: The normal-force coefficient vs. the angle of attack for a delta wing of unit aspect ratio.

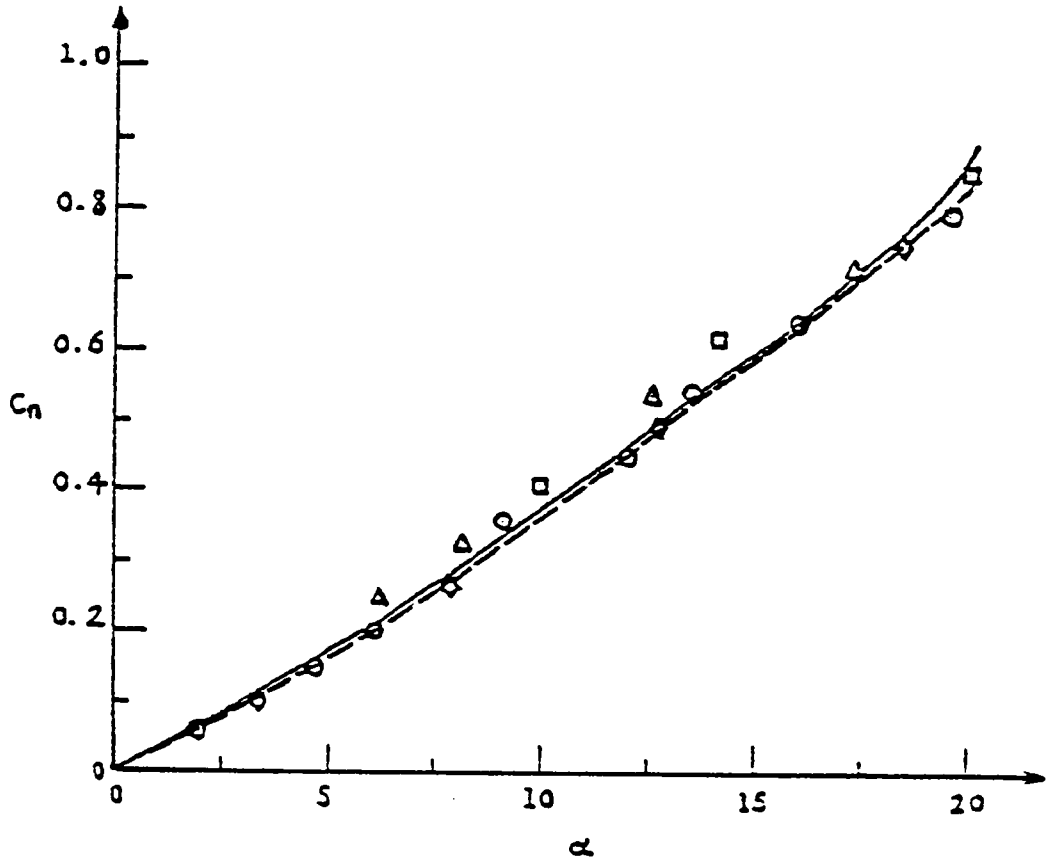

Numerical Results

□ Weber et al [45]
△ Mehrotra and Lan [46]
◇ Lamar and Gloss [47]
——— (3 rows) } Present method
— — — (4 rows) }

Experimental Results

○ Wentz [48]

Figure 13: The normal-force coefficient vs. the angle of attack for a delta wing of 1.46 aspect ratio.

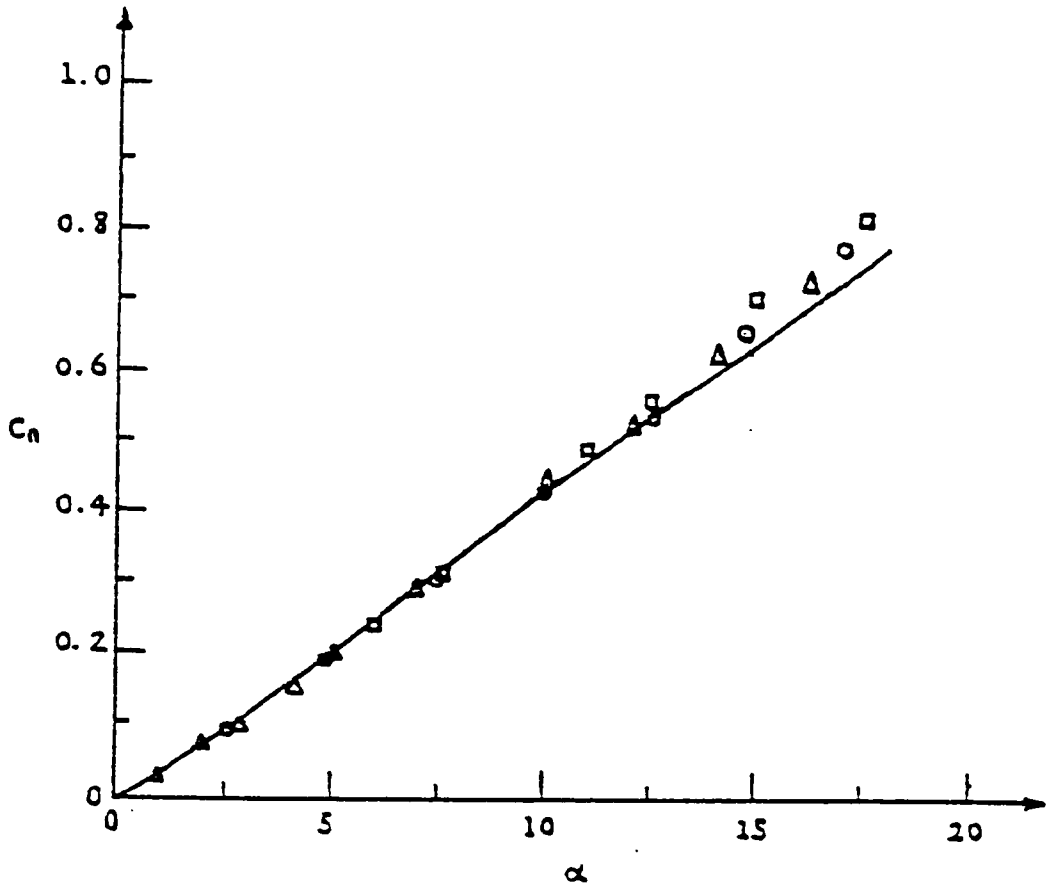

Numerical Results

□ Kandil et al [26]
——— Present method (3 rows)

Experimental Results

△ Peckham [2]
○ Bergesen and Porter [49]

Figure 14: The normal-force coefficient vs. the angle of attack for a delta wing of 1.67 aspect ratio.

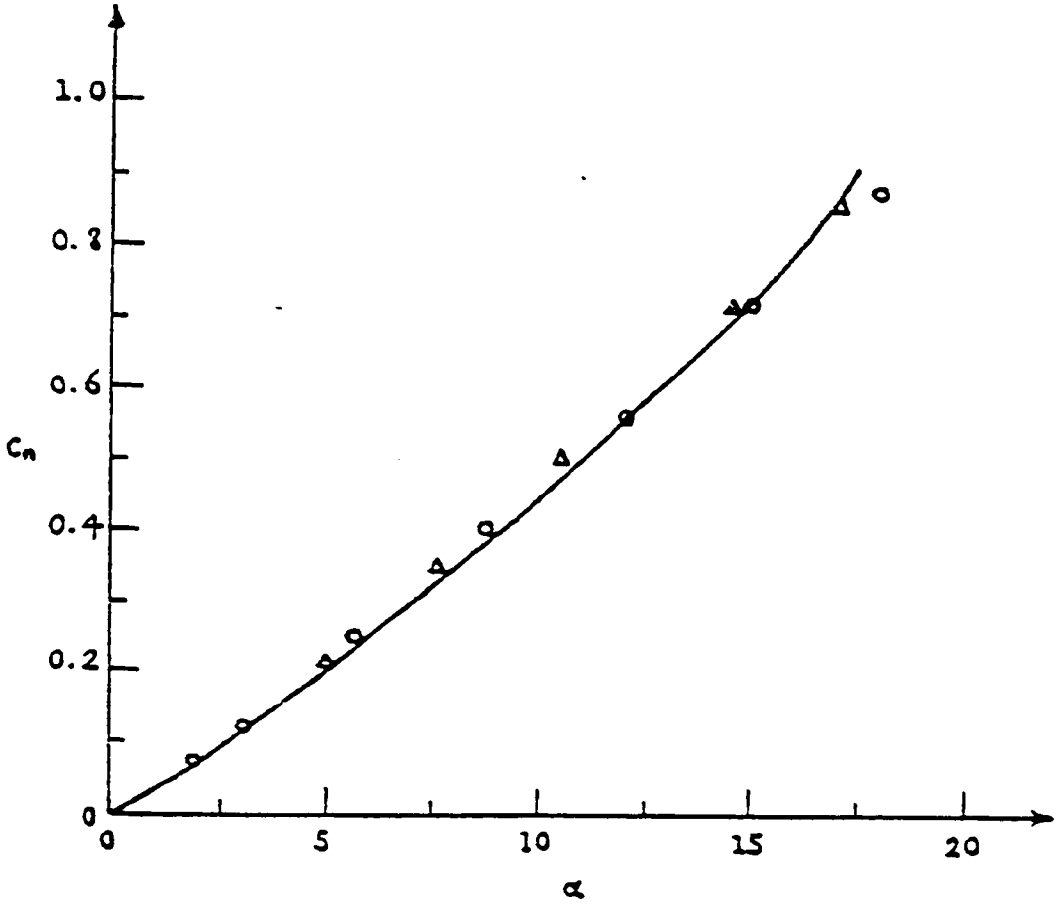

Numerical Results

△ Kandil et al [26]
———Present method (3 rows)

Experimental Results

○ Bartlett and Vidal [50]

Figure 15: The normal-force coefficient vs. the angle of attack for a delta wing of 2.0 aspect ratio.

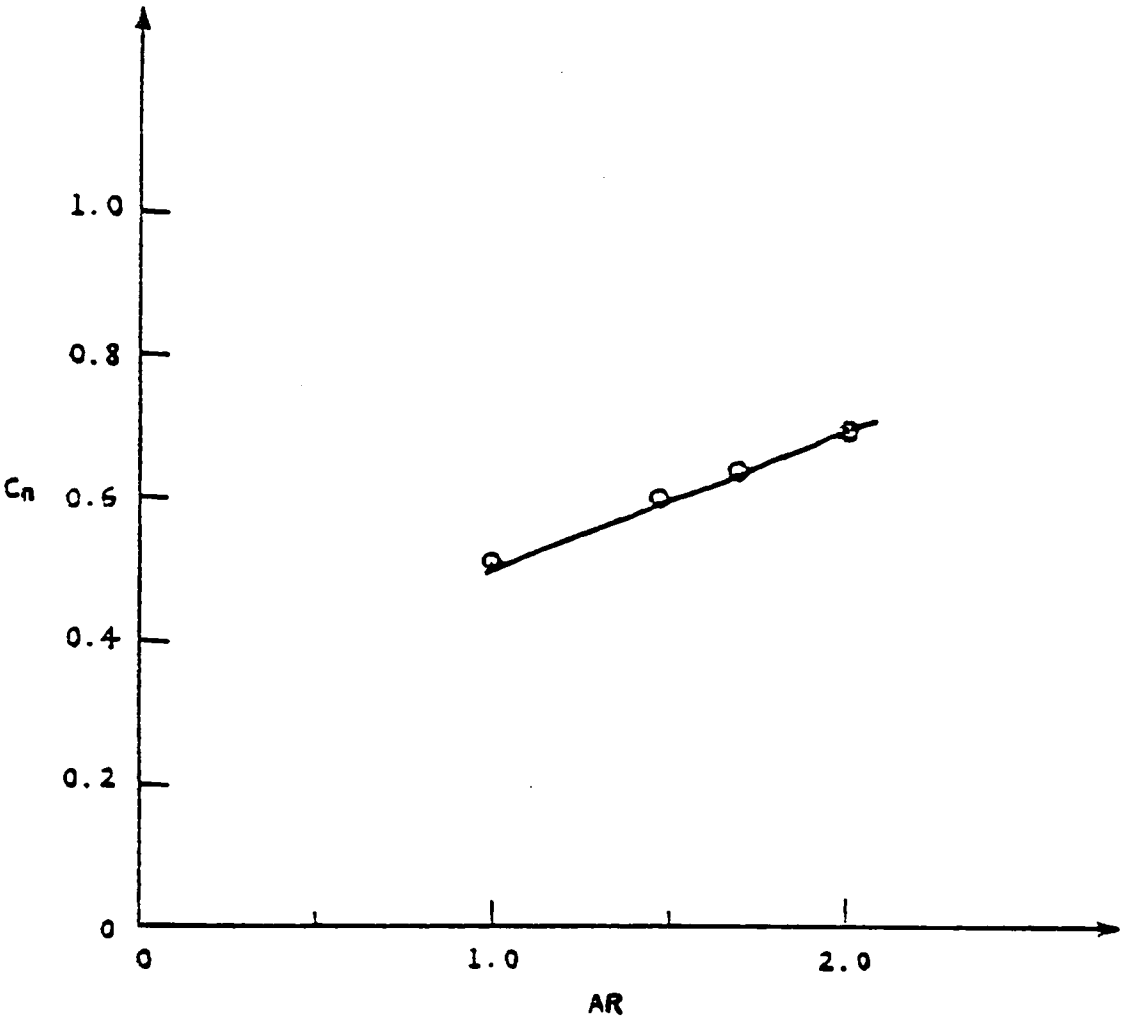

Figure 16: The normal-force coefficient vs. the aspect ratio for a delta wing at 15° angle of attack.

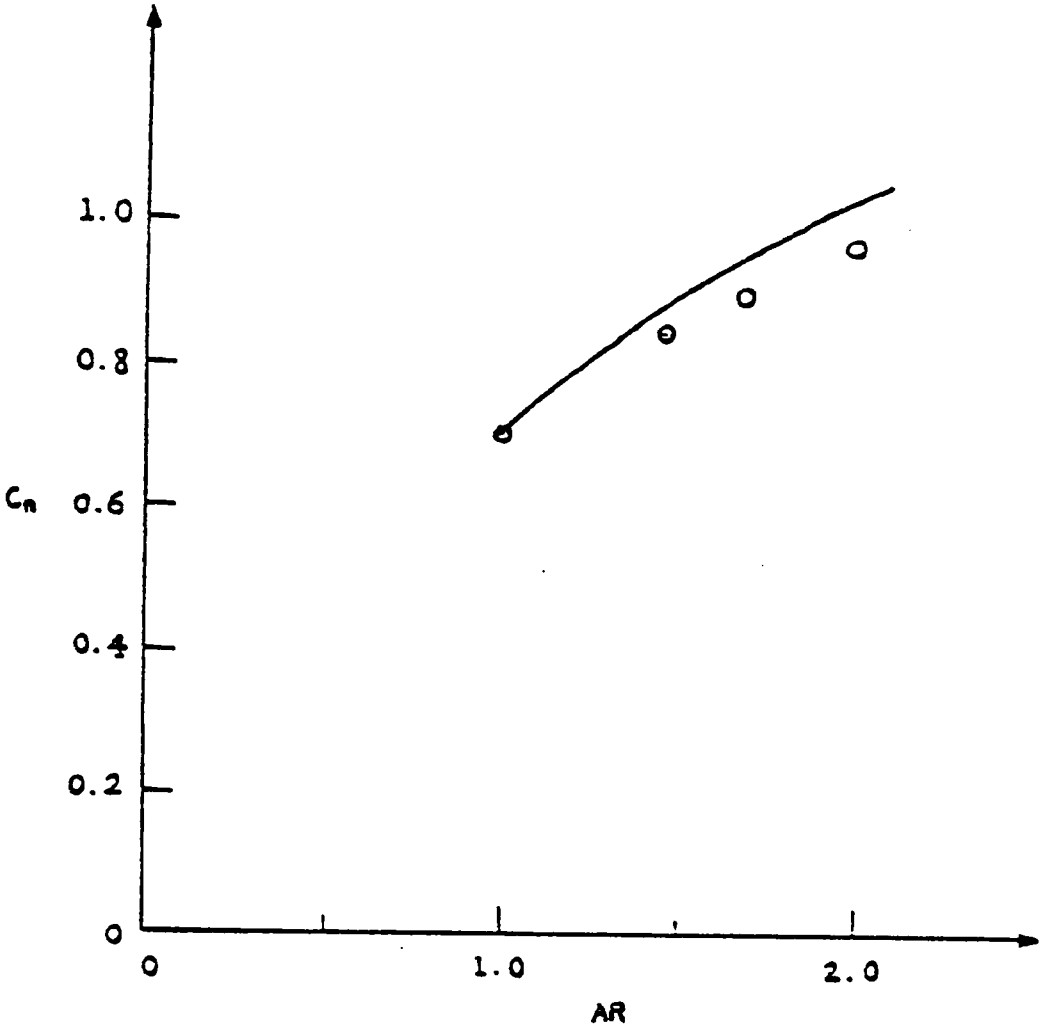

Numerical Results

o Lamar and Gloss [47]
———Present method (3 rows)

Figure 17: The normal-force coefficient vs. the aspect ratio for a delta wing at 20° angle of attack.

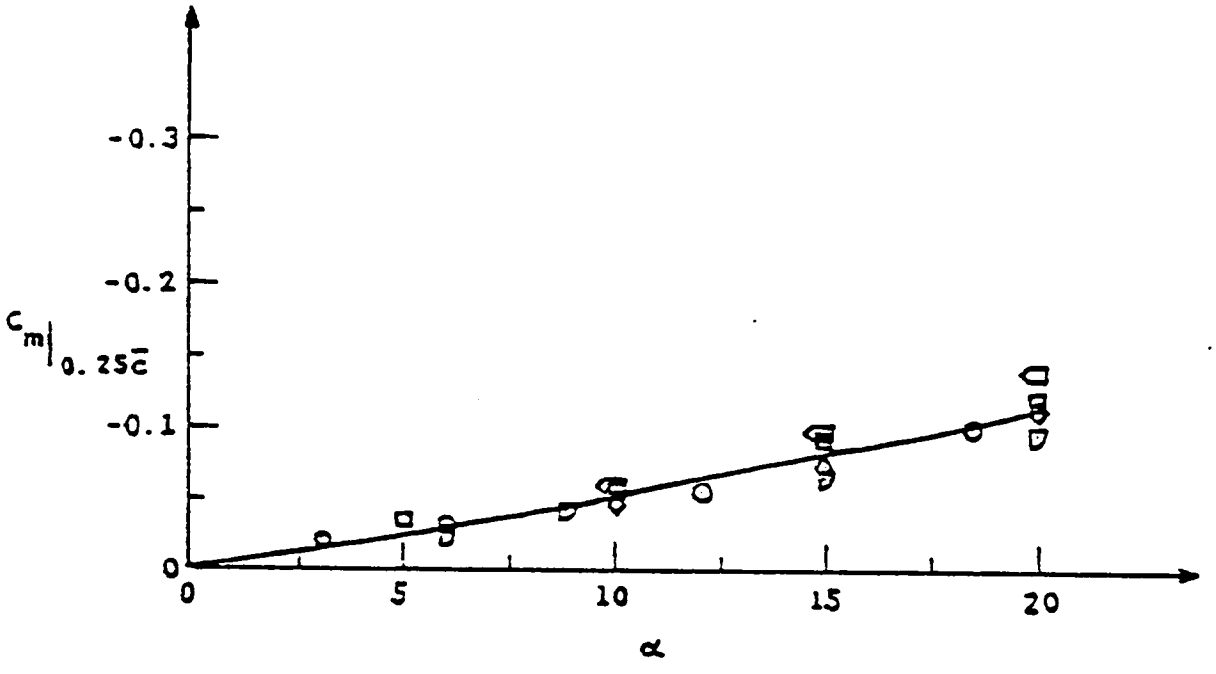

Numerical Results

- Weber et al [45]
- Mehrotra and Lan [46]
- Lamar and Gloss [47]
- ——— Present method (3 rows)

Experimental Results

- ○ Peckham [2]
- ◇ Tosti [44]

Figure 18: The pitching-moment coefficient vs. the angle of attack for a delta wing of unit aspect ratio.

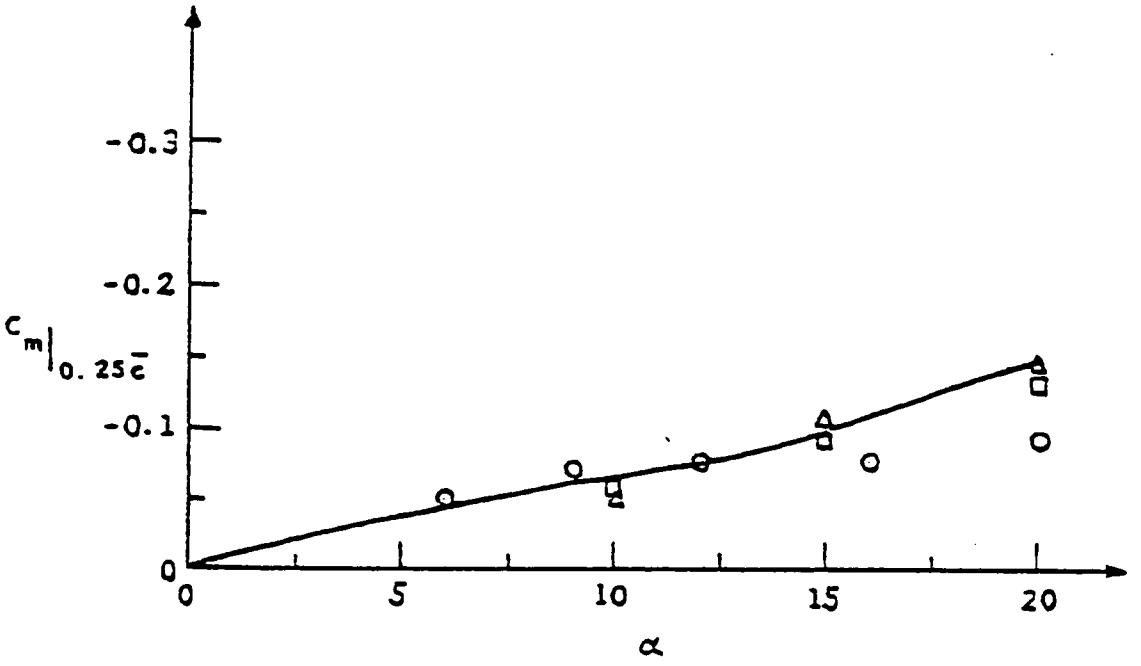

Numerical Results

□ Weber et al [45]
△ Mehrotra and Lan [46]
——— Present method (3 rows)

Experimental Results

○ Wentz and Kohlman [48]

Figure 19: The pitching-moment coefficient vs. the angle of attack for a delta wing of 1.46 aspect ratio.

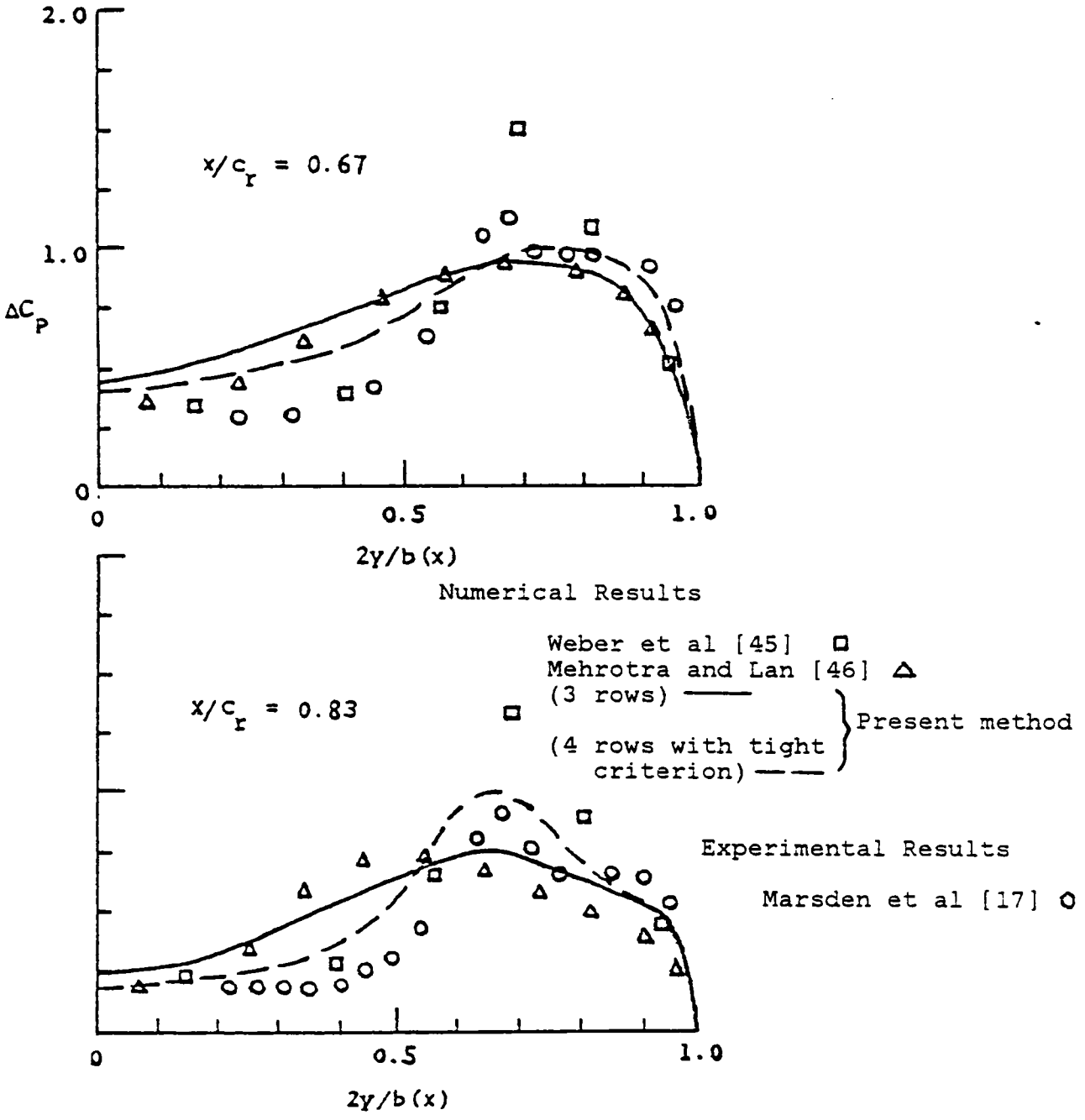

Figure 20: Spanwise pressure distributions for a delta wing of 1.46 aspect ratio at 14° angle of attack.

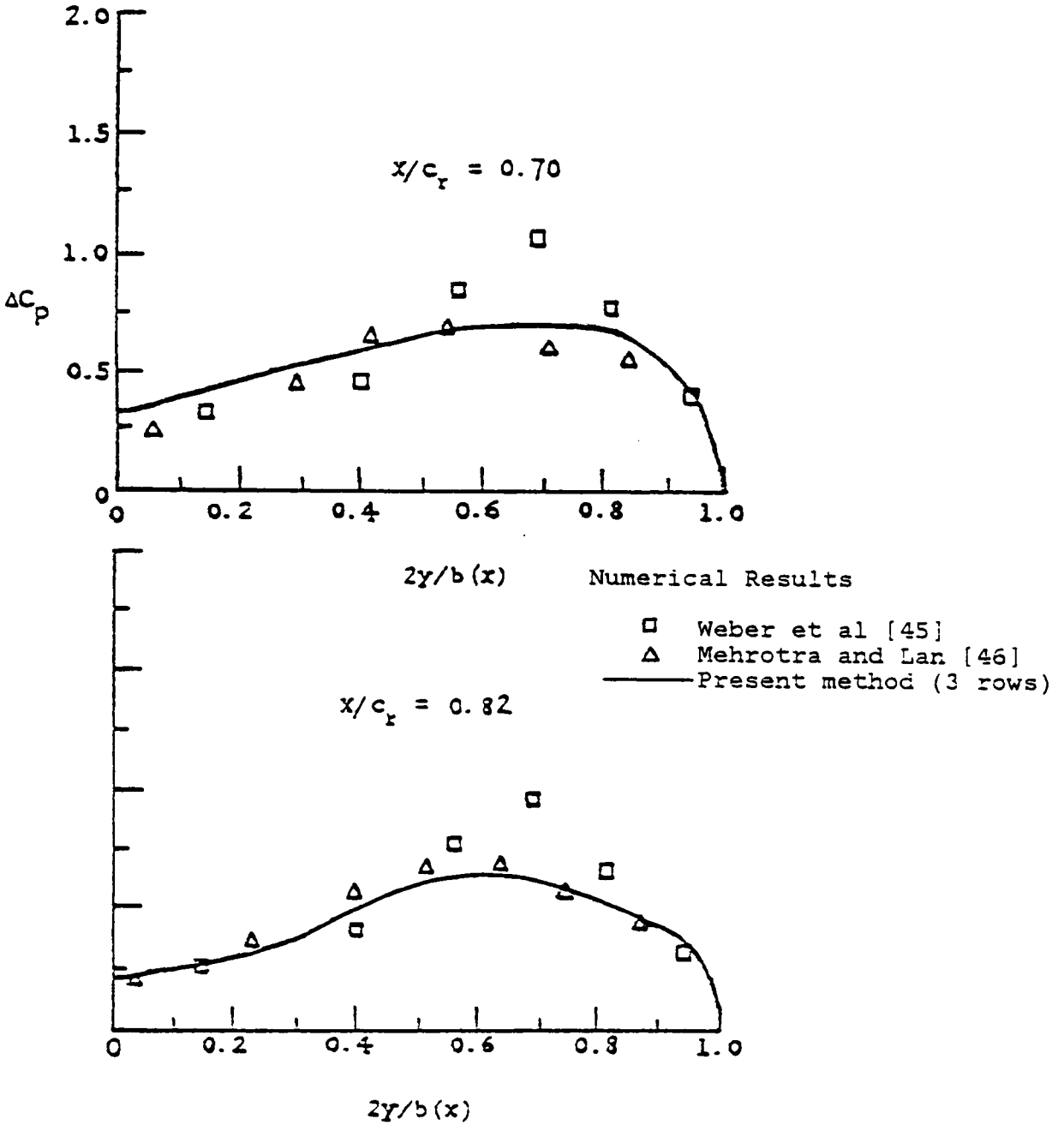

Figure 21: Spanwise pressure distributions for a delta wing of unit aspect ratio at 15° angle of attack.

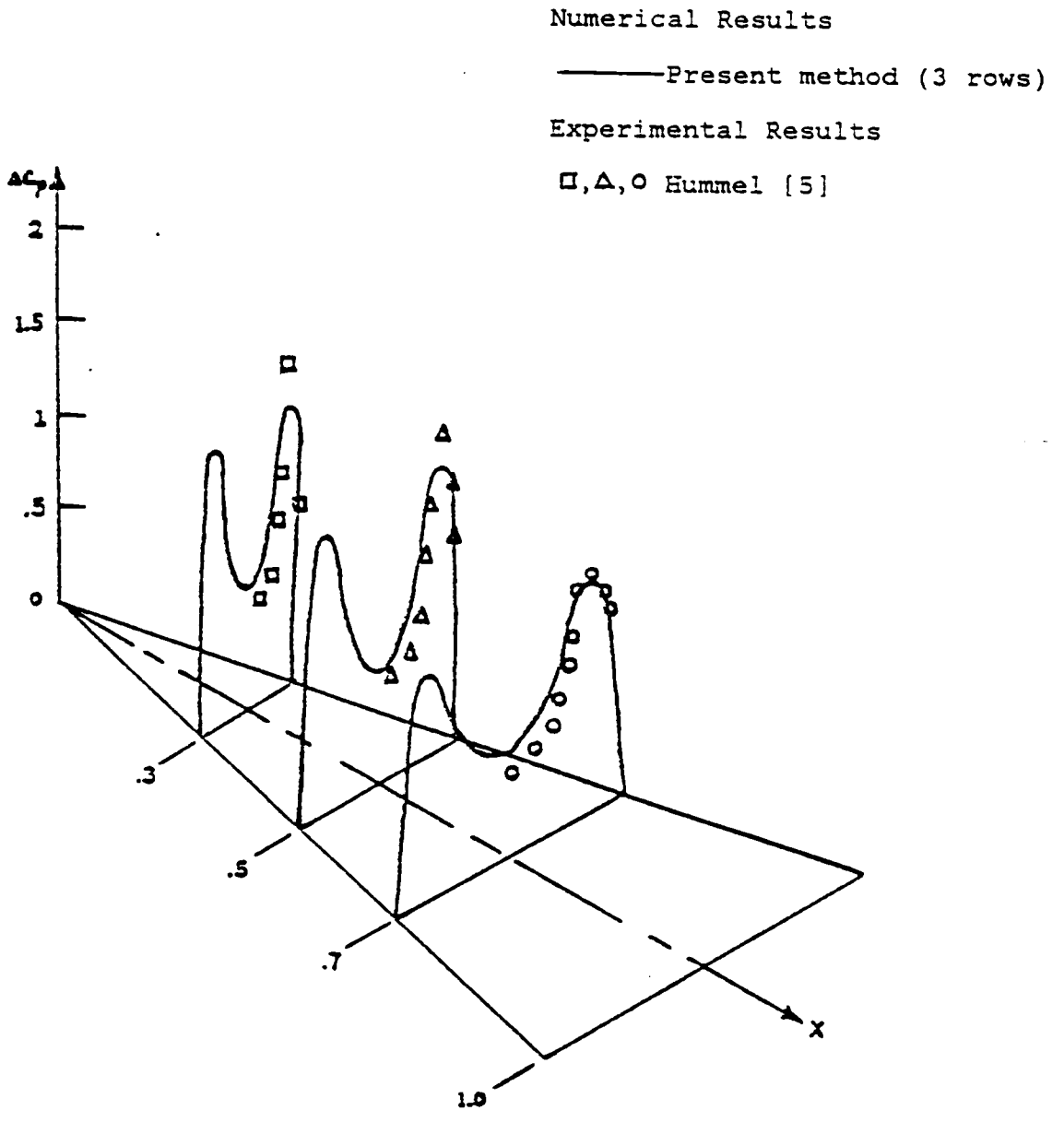

Figure 22: Spanwise pressure distributions for a delta wing of unit aspect ratio at 20° angle of attack.

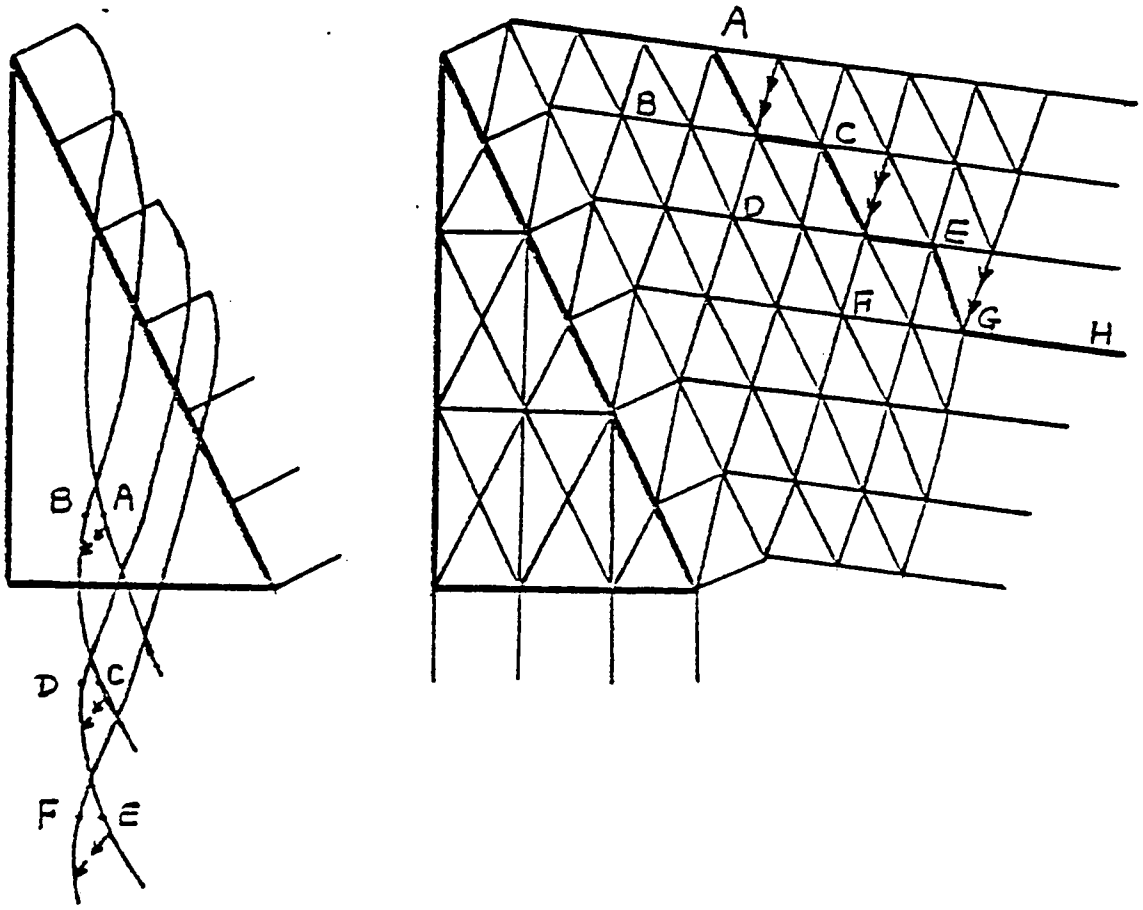

Figure 23: The arrangement of the vortex core under the tight criterion.

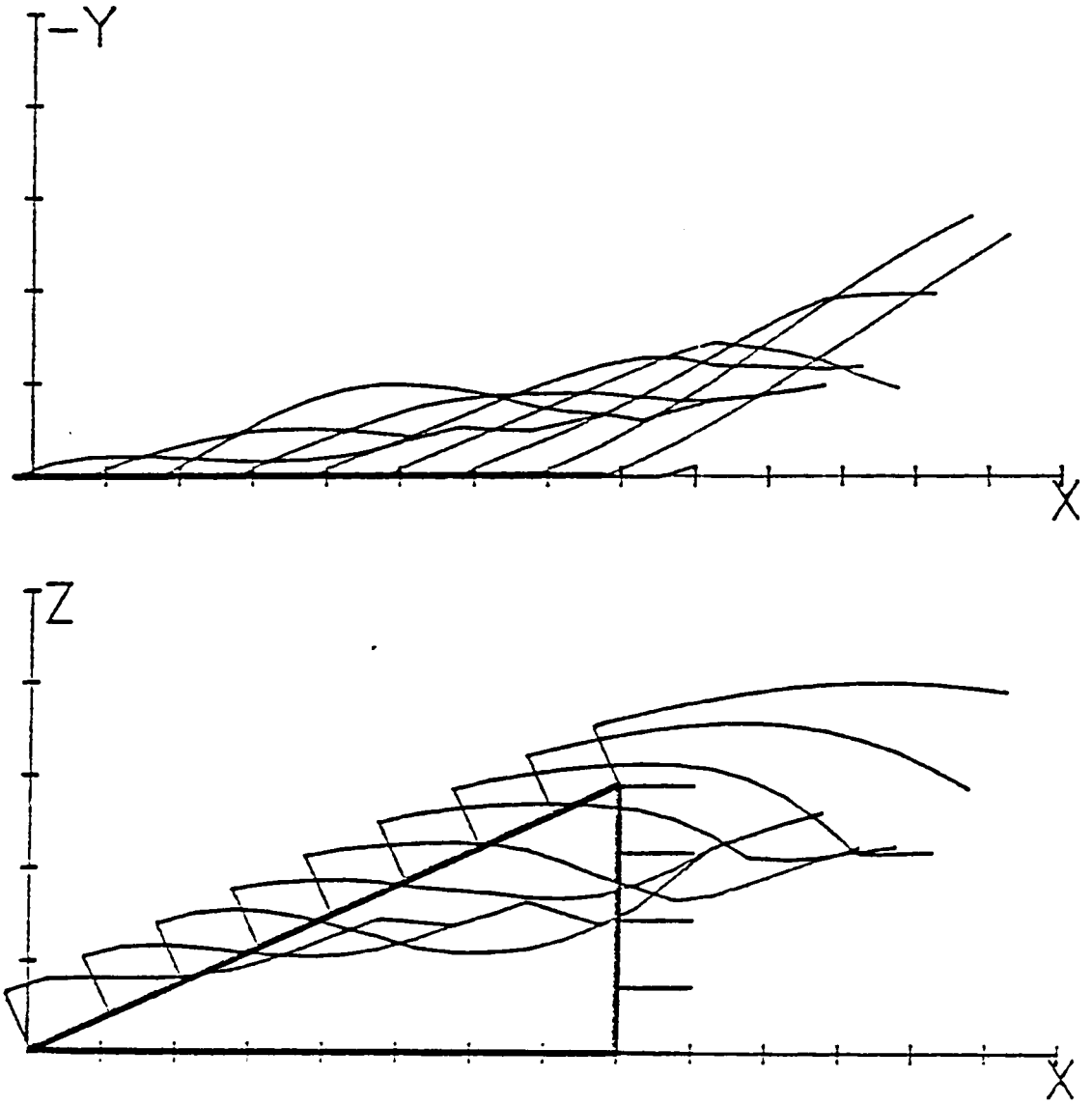

Figure 24: Solution for a delta wing by using the tight criterion for the vortex core: AR=1.46, 14° angle of attack.

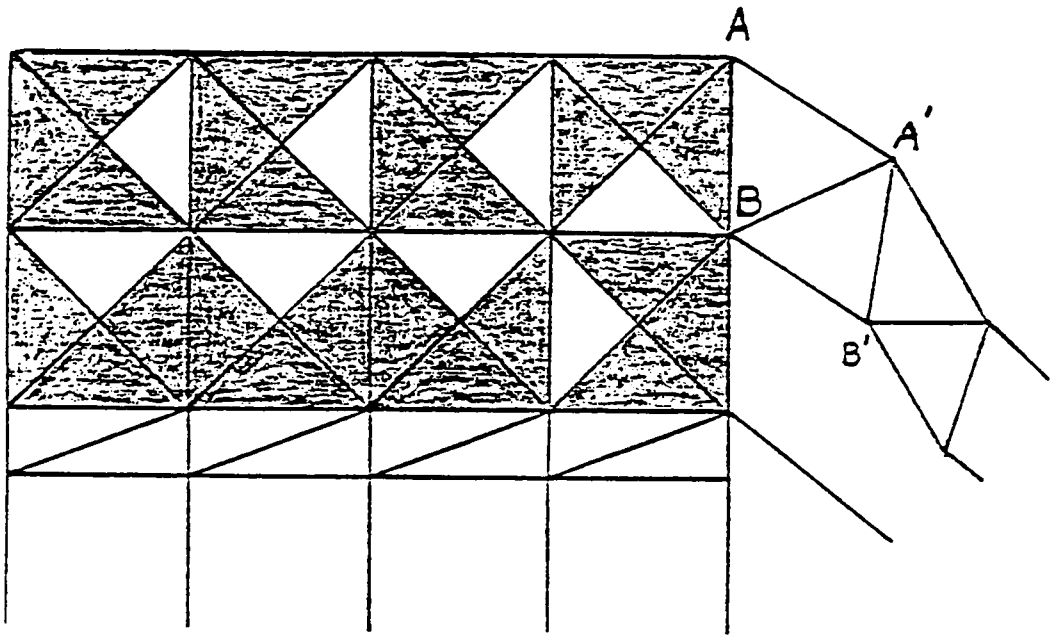

Figure 25: The arrangement of the panels for a rectangular wing.

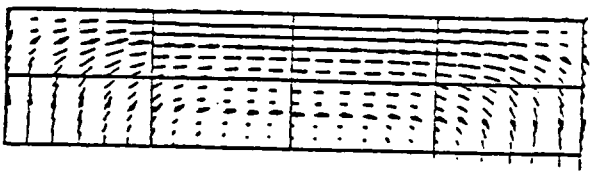

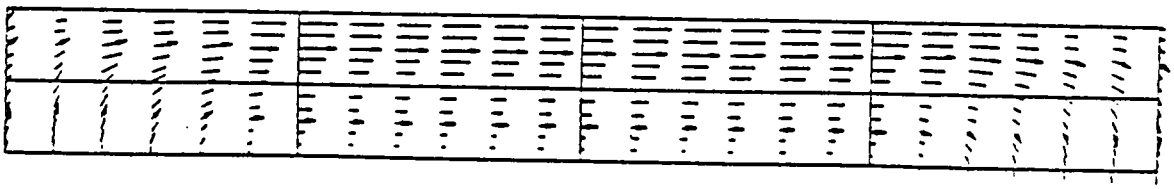

Figure 26: Vorticity fields for rectangular wings of AR=4 and AR=8 at 15° angle of attack with core at wing tip.

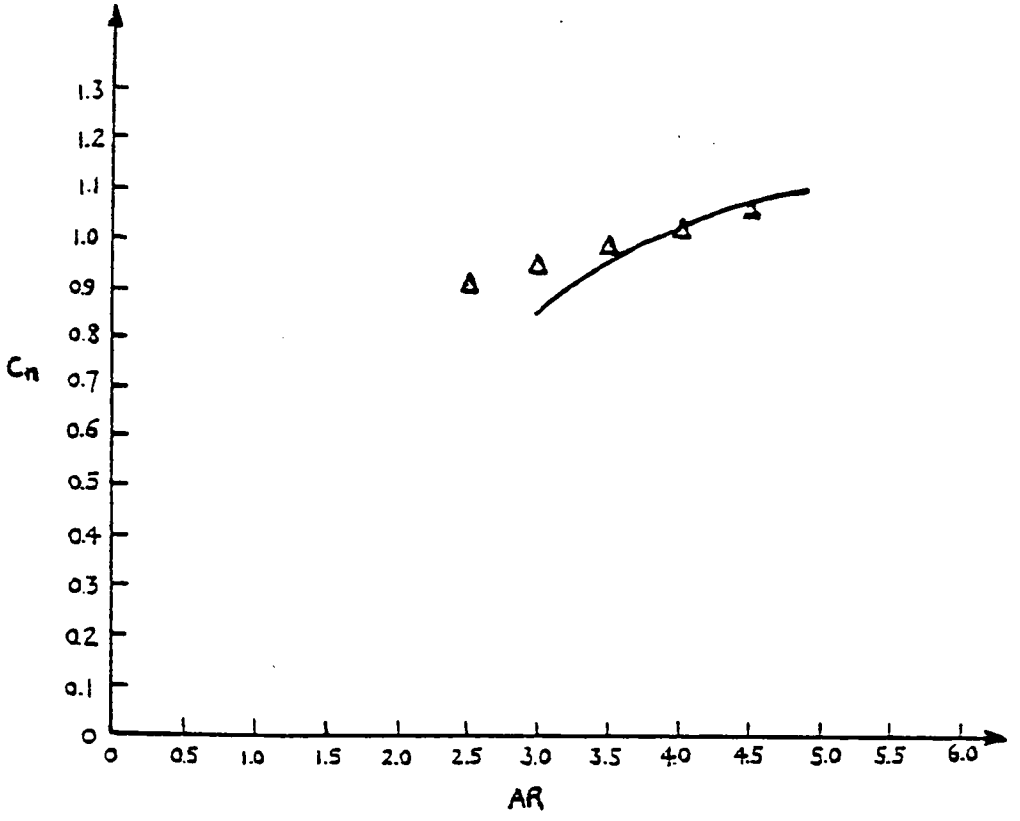

Numerical Results

———Present method

Experimental Results

Δ Winter [55]

Figure 27: Normal-force coefficient vs. the aspect ratio for a high-aspect rectangular wing at 15° angle of attack with core at wing tip.

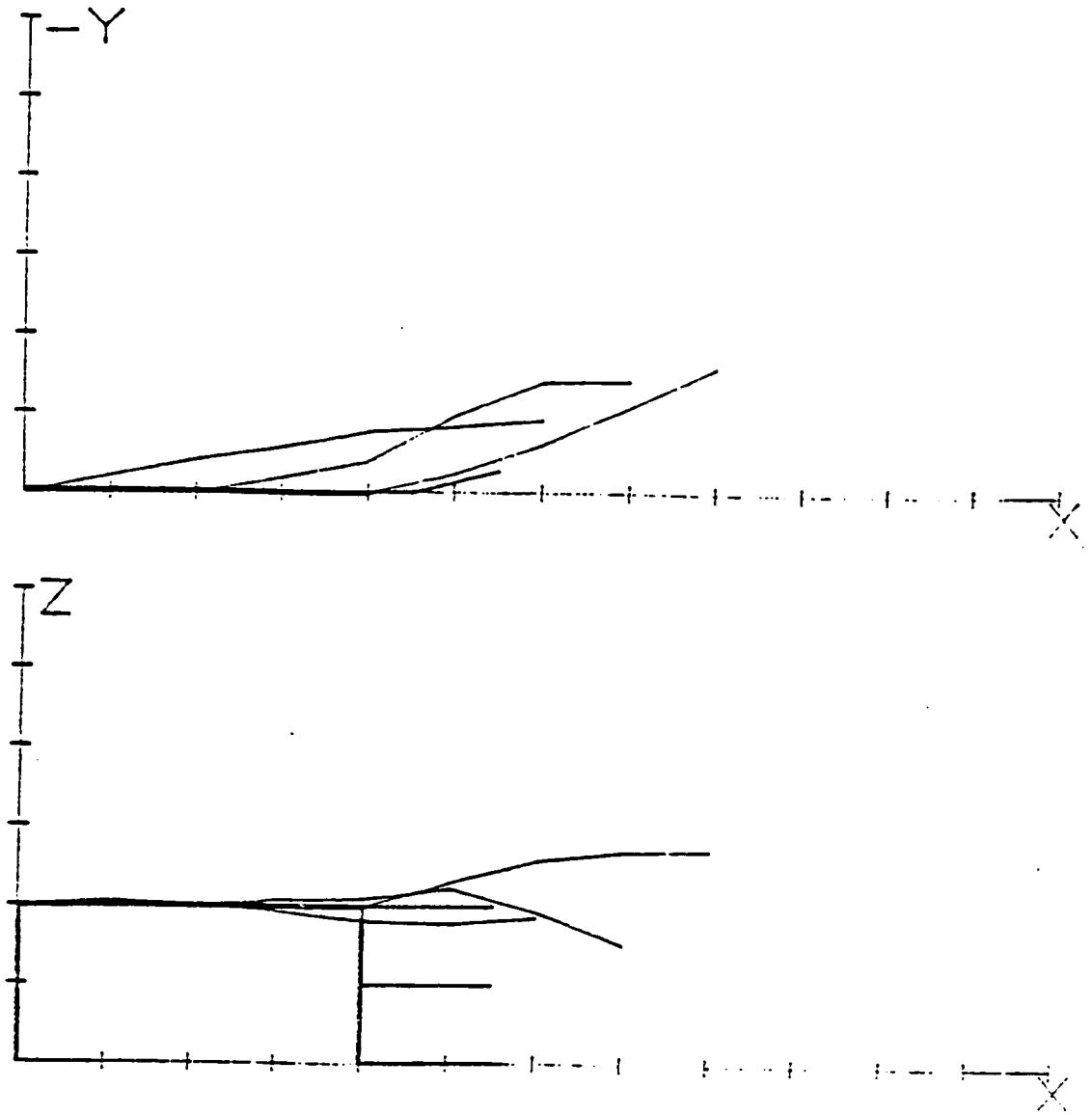

Figure 28: Solution for a rectangular wing obtained by the present method: AR=1, 15° angle of attack.

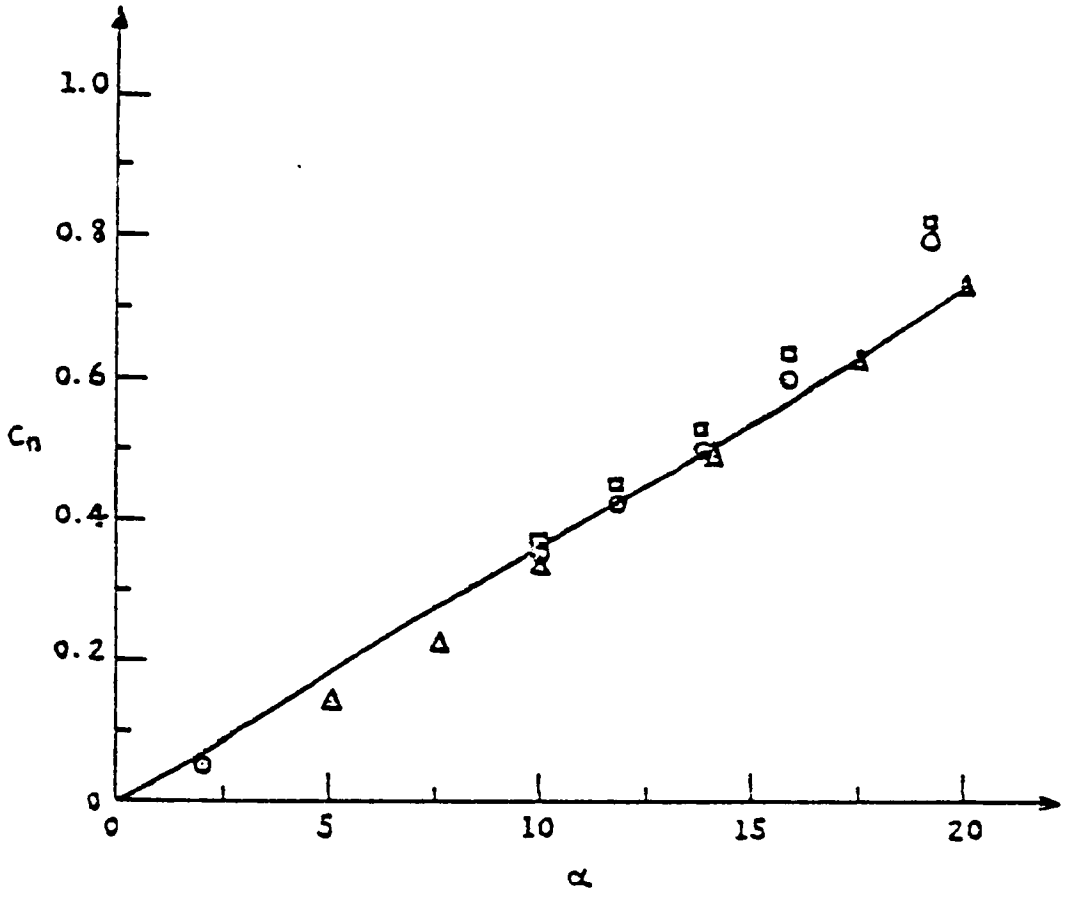

Figure 29: The normal-force coefficient vs. the angle of attack for a rectangular wing of unit aspect ratio.

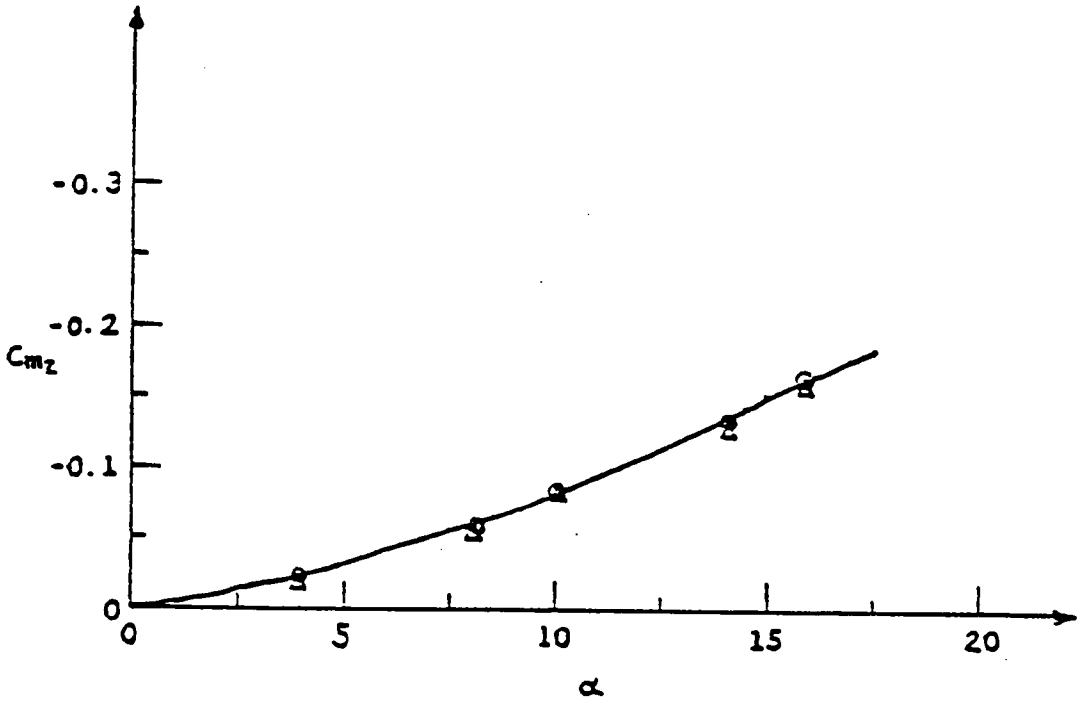

Numerical Results

△ Kandil [25]

——— Present method

Experimental Results

○ Ermolenko [52]

Figure 30: The pitching-moment coefficient vs. the angle of attack for a rectangular wing of unit aspect ratio.

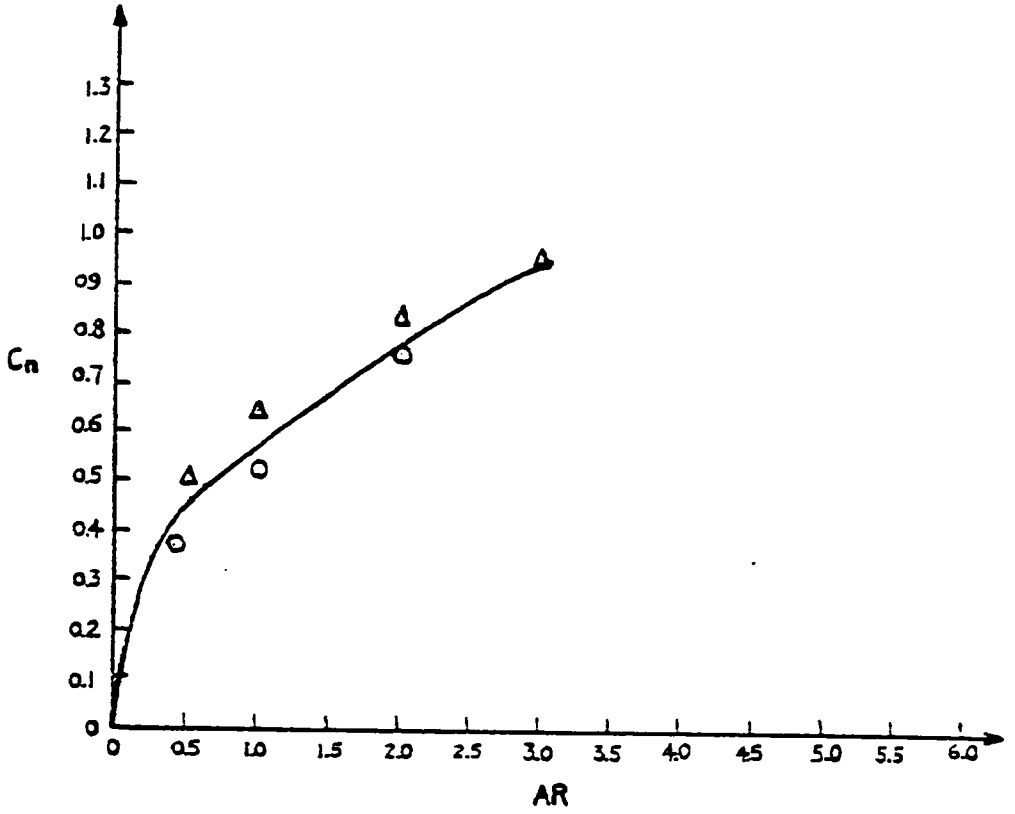

Numerical Results

Δ Kandil [25]

——— Present method

Experimental Results

o Lamar [54]

Figure 31: Normal-force coefficient vs. the aspect ratio for a low-aspect rectangular wing at 15° angle of attack.

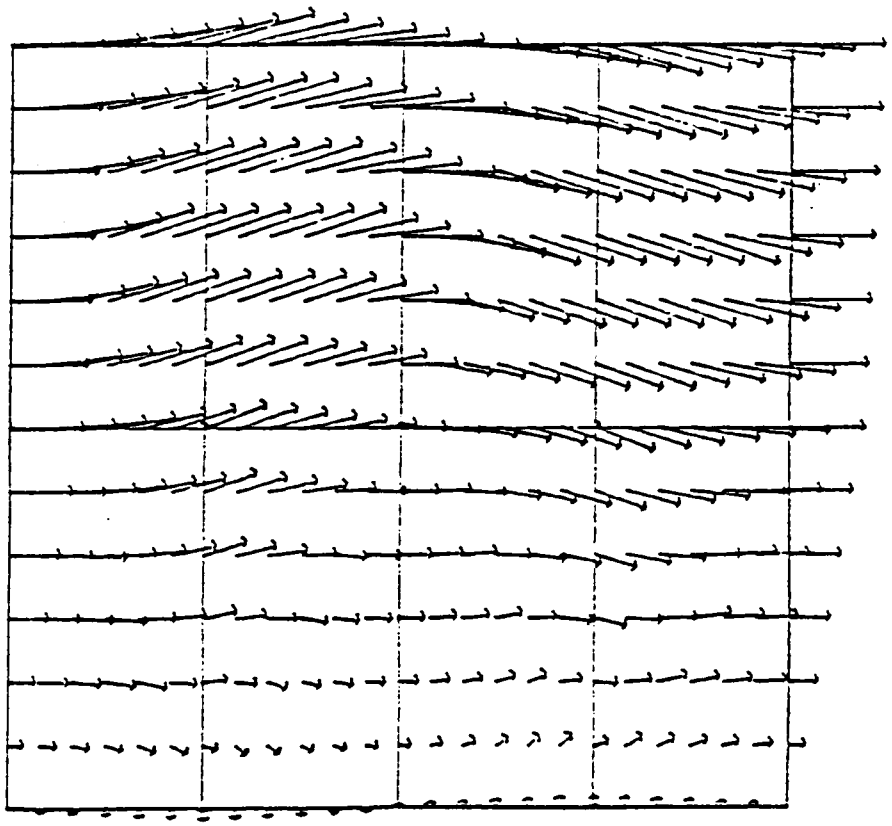

Figure 32: Vorticity field for a rectangular wing with vortex sheet attached to the wing tip, AR=1, angle of attack 15°.

The vita has been removed from the scanned document

A CONTINUOUS VORTICITY PANEL METHOD FOR THE PREDICTION OF STEADY AERODYNAMIC LOADS ON LIFTING SURFACES

ALBERT TIENGTSUNG YEN

(ABSTRACT)

A continuous vorticity panel method is developed and utilized to predict the steady aerodynamic loads on lifting surfaces having sharp-edge separation. Triangular and semi-infinite panels with linearly varying vorticity are used. The velocity field generated by an individual element is obtained in closed form. A concentrated core of vorticity is employed to simulate the leading-edge-vortex core and its feeding sheet. An optimization scheme is constructed for finding the vorticity at the nodes of the elements. The method is not restricted by aspect ratios, angles of attack, planforms, or camber. The numerical results are in good agreement with the experimental data for both rectangular and delta wings for incompressible flows.